PRESSURE GRADIENTS IN THE INNER SURF AND OUTER SWASH ZONE: A LABORATORY AND NUMERICAL INVESTIGATION

by

Autumn Noel Kidwell

A thesis submitted to the Faculty of the University of Delaware in partial fulfillment of the requirements for the degree of Master of Civil Engineering

Summer 2011

PRESSURE GRADIENTS IN THE INNER SURF AND OUTER SWASH ZONE: A LABORATORY AND NUMERICAL INVESTIGATION

by
Autumn Noel Kidwell

Approved: _____
Jack A. Puleo, Ph.D.
Professor in charge of thesis on behalf of the Advisory Committee

Approved: _____
Harry W. Shenton, Ph.D.
Chair of the Department of Civil and Environmental Engineering

Approved: _____
Babatunde A. Ogunnaike, Ph.D.
Interim Dean of the College of Engineering

Approved: _____
Charles G. Riordan, Ph.D.
Vice Provost for Graduate and Professional Education

ACKNOWLEDGMENTS

I would like to thank Mike Davidson for his invaluable technical assistance, Alec Torres-Freyermuth and the Instituto de Ingenieria, Universidad Nacional Autonoma de Mexico for hosting me during a research trip and for the assistance with COBRAS, and Jack A. Puleo for being a great advisor over the past two years.

This work was supported by the National Science Foundation through a Graduate Research Fellowship to Autumn Kidwell and through NSF grant OCE-0845004.

TABLE OF CONTENTS

LIST OF TABLES

LIST OF FIGURES

ABSTRACT

A need exists to understand better coastal processes emphasizing coastal sediment transport. Morphologic variability of shorelines is partially controlled by surf and swash-zone processes. Sediment is transported in the surf and swash zone due to a combination of hydrodynamic elements. The primary mechanisms are the wave characteristics, sediment characteristics and the beach slope. All of these can be categorized as boundary conditions which are imposed on the swash zone by the underlying bed and the surf zone.

One possible improvement to models predicting the sediment transport is the inclusion of a pressure gradient term. For this term to be considered important, a thorough lab and model investigation is detailed in this thesis. The presence and magnitude of total pressure gradients is investigated. To do this, a measurement technique that incorporates the total pressure under a wave was developed. The experimental results were compared with the results of a robust 2D numerical model for the test case of a solitary wave propagating over a 'typical' beach face.

10 solitary wave tests were conducted in a laboratory wave flume to investigate the horizontal pressure gradient under a wave. These experimental tests showed that using the nearbed pressure sensors instead of a proxy yielded a higher shoreward pressure gradient in the surf zone under a passing wave. The numerical model performed well in predicting the experimental pressure gradient and provided a more spatially detailed analysis of the importance of the pressure gradient as the wave propagates through the surf and swash zones.

Chapter 1

OVERVIEW OF SURF AND SWASH ZONE

The United States is bounded by over 152,000 kilometers of coastline. In 2003, 53% of the nation's population lived in coastal counties accounting for 17% of the country's land area (Crossett et al, 2004). The US coastal population is growing at a rate that is larger than the national average. Unfortunately, nearly 85% of the sandy coastlines are eroding (Thornton et al., 2000). These coastal changes will significantly affect the lives of many Americans. As global climate changes, sea level is expected to continually rise by rates between 0.1 to 0.3centimetersper year (Crossett et al, 2004). While these rates may seem insignificant, horizontal shoreline transgression is considerable when considered over a shallow sloping coastal zone. Over time, hundreds of meters of beach are lost and coastal communities and entire wildlife habitats are inundated. With rising sea level and the occurrence of more severe storm events, the effect of shoreline change on coastlines will be exacerbated. There is an imminent need to understand better coastal processes, with specific emphasis on coastal sediment transport.

A global commonality for all shorelines is that their morphologic variability is partially controlled by surf and swash-zone processes. The surf zone is commonly defined as shoreward of the wave break-point (Figure 1.1). The swash zone is the part of the beach profile that is alternately covered and uncovered by waves. The swash zone is defined as the portion of the beach which transitions from the minimum wave run-down and maximum wave run-up.

1.1 Significance

The swash zone is the area where waves reflect or dissipate their energy after traversing through the surf zone. After breaking, waves are transformed to different types and scales of motion with both large and small scale turbulence, low frequency waves, and steady flow conditions. It is a key region for shoreline evolution, is often the location where beach erosion occurs and is the lateral boundary for oceanic processes affecting land. Due to the fact that waves and storms release a large portion of their energy in the swash zone, the ability to predict accurately sediment transport in the swash zone is crucial for beach nourishment projects, flood mitigation, and planning of future coastal infrastructure.

1.2 State of Research

1.2.1 Hydrodynamics

Sediment is transported in the surf and swash zone due to a combination of hydrodynamic elements. The primary mechanisms are the wave characteristics, sediment characteristics and the beach slope. All of these can be categorized as boundary conditions which are imposed on the swash zone by the underlying bed and the surf zone.

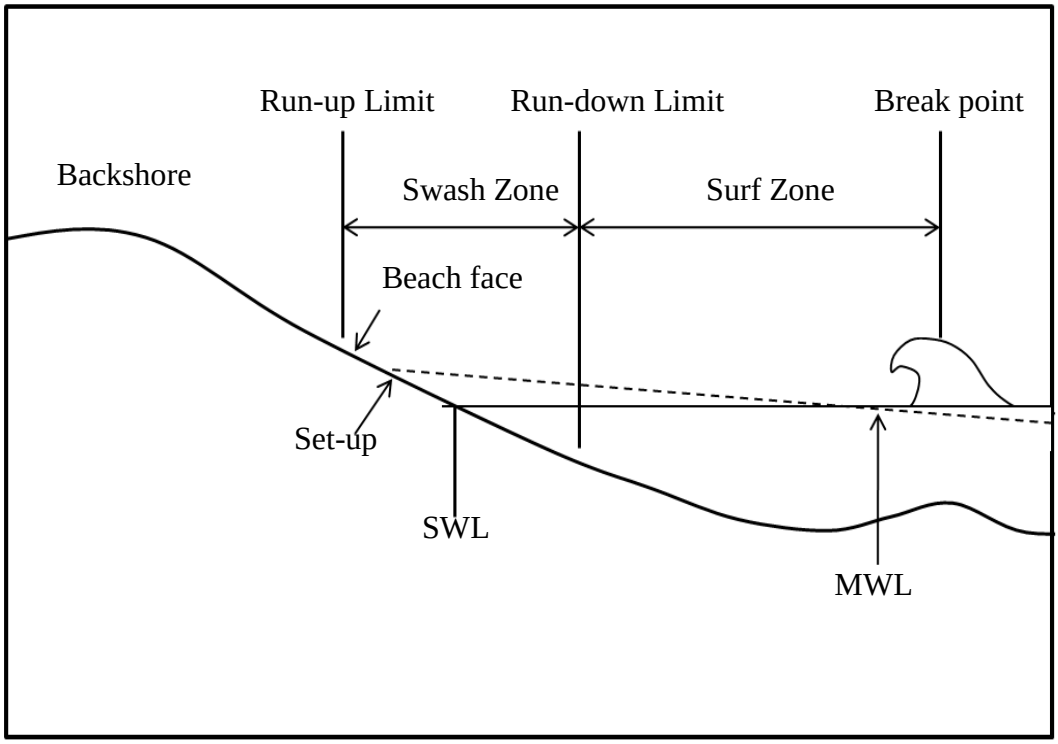

Figure 1.1: This schematic is a simple illustration of the regions of interest for this study on the inner surf and outer swash zones.

The dominant boundary condition for the swash zone is the hydrodynamics of the inner surf zone, since it is the seaward edge of the swash zone (Elfrink and Baldock, 2002). Therefore, this boundary needs to be well-defined in order to better understand and predict swash-zone processes.

The inner surf zone can be characterized by different types of fluid motions including edge waves, short waves, long waves, cross-shore and long-shore currents, etc. The prevalent fluid motion is highly dependent upon the beach characteristics. In the case of a mild-sloping beach, the dominant motion will

generally be a non-breaking low frequency wave (infragravity wave). When the surf conditions are unsaturated, there can be more short wave energy with a wave bore which reaches the shoreline (Battjes, 1988). A saturated surf zone occurs when the short wave heights are depth-limited and an unsaturated surf zone occurs when the wave heights are independent of the water depth. The different surf zone conditions are often parameterized using the Iribarren number (Iribarren and Nogales, 1949):

$$\xi_o = \beta / \sqrt{H_o / L_o} \,, \qquad 1$$

whereβ is the beach slope, H_o is the deep water wave height and L_o is the deep water wave length. For an Iribarrennumber of less than 0.5, the surf zone has spilling breakers and is saturated. If the Iribarren number is greater than 0.5, the surf zone is typically unsaturated and has plunging breakers. The third type of breaker (collapsing) is not often investigated since the breaking occurs in one collapsing motion, no surf zone exists and the breaking does not propagate shoreward. The above distinction between the plunging and spilling breakers refers to the phase at which wave breaking begins. As the wave continues shoreward, both spilling and plunging breakers develop into a turbulent bore. The generated bore approaches the leading edge of the water, collapses and continues up the beach slope to the point of maximum run-up then reverses down the beach, defining the swash zone. Figure 1.2 shows a sequence of swash-zone velocity snapshots as output by Cornell Breaking Wave and Structures (COBRAS) numerical model. This figure provides a visual for the bore collapse and the ensuing swash motion.

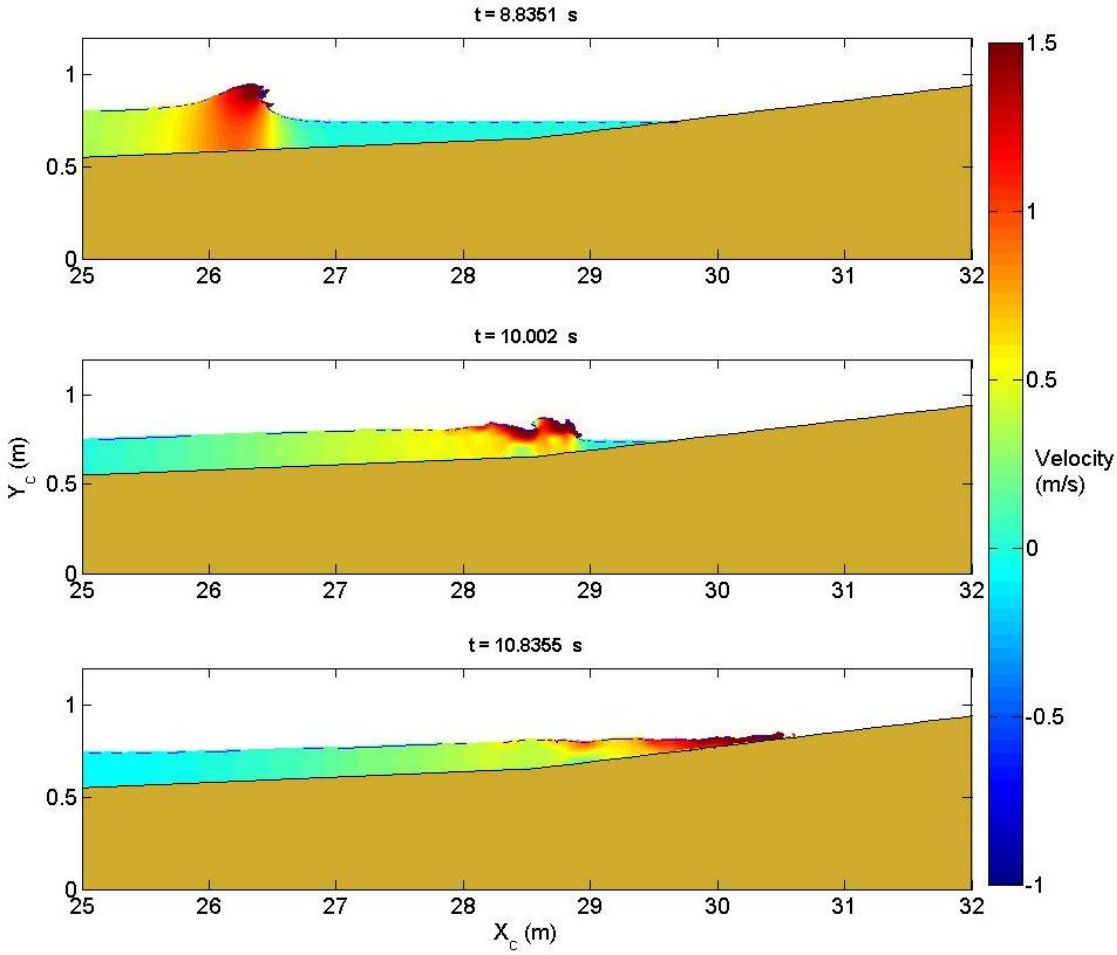

Figure 1.2: A bore collapsing and propagating through the swash zone is shown through this series of snapshots from the COBRAS model. The color scaling of the fluid is representative of the velocity field.

A simple description of the bore propagation in the swash zone is based upon the motion of a subcritical bore modeled as a fluid slab and influenced only by friction

and gravity(Figure 1.3). By conserving mass across the leading edge of the swash, the velocity of the swash,*U*, is synonymous to the particle velocity,*u*, at that location.

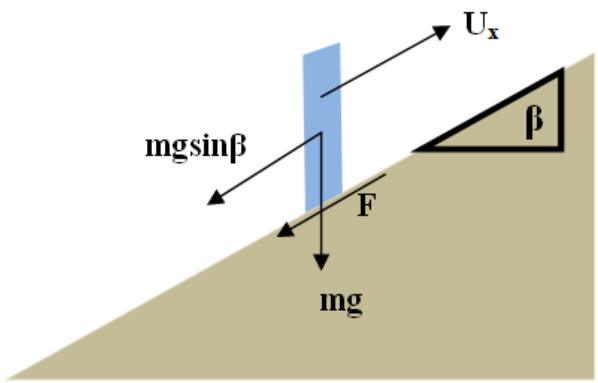

Figure 1.3: A summary of the forces acting upon a swash fluid element of length *δs* and height *δh* is illustrated propagating along a beach face.

The force balance is given as

$$m\frac{dU}{dt} = m\frac{d^2X}{dt^2} = -mg\sin\beta - \frac{1}{2}\rho f_c |U| U \delta s \quad , \qquad 2$$

where *m* is the mass of the fluid element, *g* is gravitational acceleration, *sin β* is the beach slope, *ρ* is the density of the fluid, *fc* is the coefficient of friction between the fluid and the beach face, *U* is the fluid velocity, and *δs* is the length of the fluid element (Shen and Meyer, 1963; Hibberd and Peregrine, 1979; Kirkgöz, 1981). Several models of swash-zone kinematics been based on this type of force balance.

The hydrodynamic conditions are different during run-up and run-down. Run-up is generally characterized by a shoreward decelerating flow due to both

gravity and friction acting in opposition to the direction of the flow. During run-down, the flow accelerates due to gravity but can also experience a deceleration caused by the bed roughness. Analysis of this area is complex since run-down is not simply the reverse of run-up. Integrating equation (2) leads to equations for the run-up and run-down in the swash zone. Equations (3) and (4) show one of the derived models for the swash motion (Shen and Meyer, 1963; Kirkgöz, 1981;Puleo and, 2011).

$$X_{+}(t) = \frac{2\delta h}{f_c} \ln\left\{ \frac{\cos\left[\tan^{-1}\left(\frac{U_0\sqrt{f_c}}{\sqrt{2g\delta h \sin\beta}}\right) - t\sqrt{\frac{g f_c \sin\beta}{2\delta h}} \right]}{\cos\left[\tan^{-1}\left(\frac{U_0\sqrt{f_c}}{\sqrt{2g\delta h \sin\beta}}\right) \right]} \right\}, \qquad 3$$

$$X_{-}(t) = -\frac{2\delta h}{f_c} \ln\left[\cosh\left(\frac{-t\sqrt{g f_c \sin\beta}}{\sqrt{2\delta h}} \right) \right], \qquad 4$$

where$X_{+}(t)$ is the distance the leading edge of the swash travels in the onshore direction,$X_{-}(t)$ is the distance the leading edge travels in the offshore direction after flow reversal, t is time, andU_0 is the initial velocity at the initiation of a swash cycle. Figure 1.4 shows the variation in the swash trajectory on a 1/10 beach slope when different parameters from Equations (3) and (4) are varied.

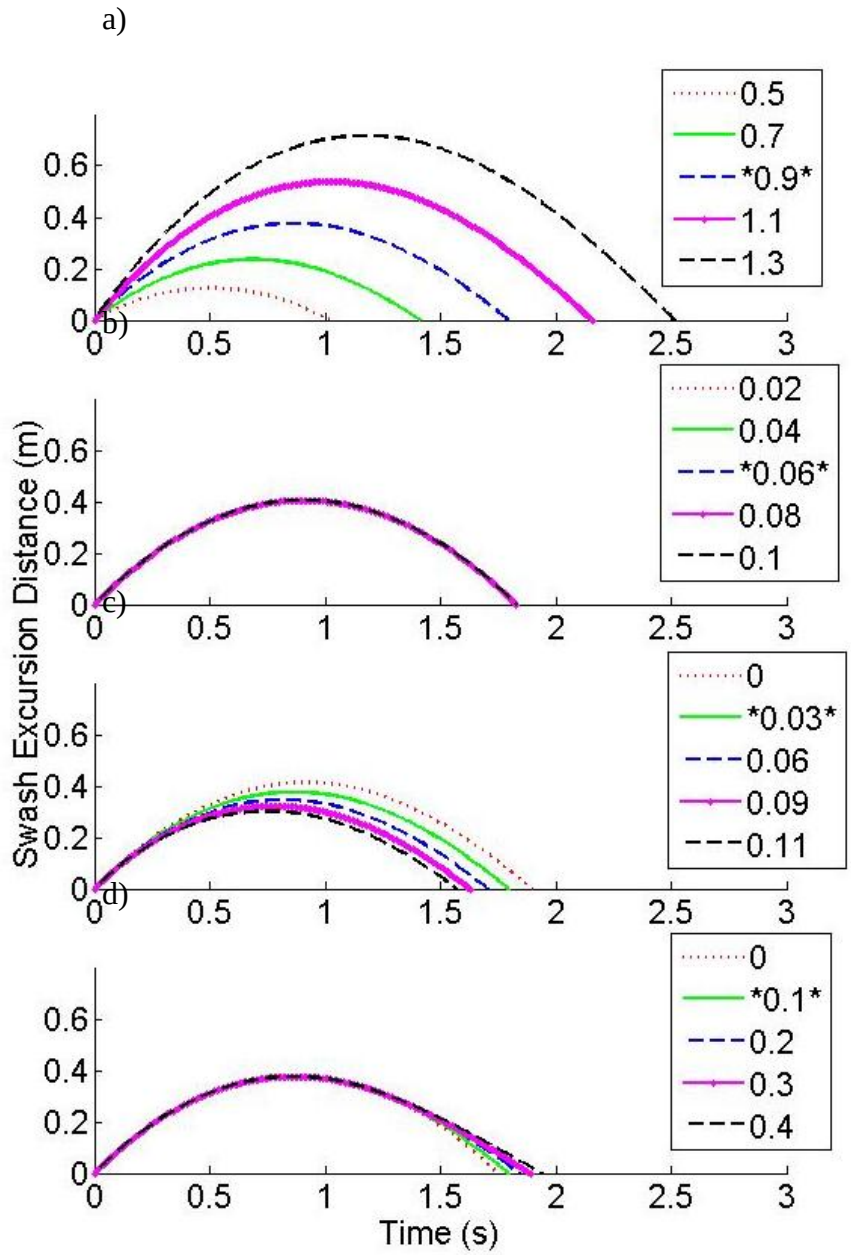

Figure 1.4: The parabolic motion of the swash zone based on Equations 3 and 4 is shown. a) variations in initial velocity U_0, b) variations in leading edge height *dh*, c) variations in the run-up friction coefficient f_c in Equation 3, d) variations in the run-down friction coefficient f_c in Equation 4.

In Figure 1.4, the velocity was varied over a range of 0.5 to 1.3 m/s, the leading edge thickness was varied from 0.02 m to 0.1 m, and the run-up and run-down friction coefficients vary from 0 to 0.11 and 0 to 0.4 respectively. The values that were held constant in each case are highlighted with asterisks in Figure 1.4, while one variable is changed in each subplot. Each range of values is based upon results from previous numerical and experimental research (Holland and Puleo, 2001;Masselink and Puleo, 2006; Shin and Cox, 2006). Changing the initial velocity over one order of magnitude effects the largest change in the excursion distance of swash flow, and the length of time for a swash event. The smallest change occurred by altering the height of the leading edge of the swash zone over one order of magnitude.

While the approach illustrated above was able to provide insight into fluid mechanics of the swash zone, a more complete description is needed. Within the swash lens, the internal flow kinematics and turbulence complicate the analysis. The swash zone is an area of high turbulence, which makes collecting data difficult. The sources of turbulence in the swash zone are the inner surf zone, bore collapse, run-down bores, and swash-swash interactions. This turbulence can lead to sediment advection, especially during run-up. During run-down, the main source of turbulence is the bed boundary. Infiltration and exfiltration of water in the beach face can also modify the bed stress that can alter the hydrodynamics and ultimately the sediment transport.

1.2.2 Sediment Transport

The sediment transport processes that occur in the inner surf and outer swash zone influence the overall beach face morphology and determine whether sand accumulates on the upper beach face or is transported offshore (Puleo et al., 2000;

Butt et al., 2007). The preceding section showed that this region is hydrodynamically complex. This complexity is made evident in the efforts to understand better sediment transport. As mentioned, the hydrodynamic conditions vary during run-up and run-down. Also, depending upon the beach grain size and saturation, infiltration into the beach face is prevalent during run-up and exfiltration is associated with run-down. These processes have the ability to mobilize sediment particles and influence bed shear stresses (Butt et al., 2000; Turner and Masselink, 1998).

Sediment transport in the nearshore is classically separated into two components: bedload and suspended load. Bedload is the portion of the transported sediment that is supported by the intergranular forces of the individual sediment particles. Suspended load is part that is supported by fluid drag (Bagnold, 1956). Horn and Mason (1994) investigated the relative importance of the two terms experimentally using a compartmentalized sediment trap. The cutoff between suspended load and bedload was 1cm above the bed. The study was conducted at four beaches. The bedload transport was greater than suspended transport at three beaches during run-down. At two of the beaches, the bedload was also greater than the suspended load during run-up as well as run-down. They found that the sediment transport varied with the phase of the swash cycle. For run-up, the sediment transport is a combination of suspended load and bedload, and for run-down, the main mode of sediment transport is bedload. These variations in transport need to be accounted for when modeling swash zone sediment transport. Not only is it uncertain as to whether the sediment transport should be divided into two components, but it is difficult to measure and predict the movement of sediment regardless of classification (Masselink and Hughes, 1998).

Since the hydrodynamics of run-up are different than run-down, it is logical that the sediment transport is also different for each part of the swash cycle. During run-up, the swash has an initial velocity and decelerates until maximum shoreward excursion is reached. When the flow reverses, the swash begins with a zero velocity and accelerates seaward. The flow velocity, suspended sediment concentrations and suspended fluxes are maximum at the onset of run-up where turbulence is prevalent. The turbulence stirs up the particles suspending them higher into the water column. Swash flow rapidly expends energy as it nears the maximum excursion and the particles of sediment settle out of the swash lens by the time the flow reverses. The run-down is generally less turbulent than run-up, since it does not have the surface generated turbulence of a collapsing bore, yet the flow can be supercritical generating a turbulent hydraulic jump. The turbulence during run-down is generally bed generated, and most of the transported material stays close to the bed and is often classified as bedload (Mason, 1994; Butt and Russell 1991; Puleo et al, 2000).

Many swash-zone sediment transport models rely on the energetics formulation first postulated by Bagnold (1963). The premise is that when the flow of the swash zone extends over the beach, some energy is transferred from the fluid to the sediment through shear stress, thereby mobilizing and transporting sediment. A quadratic drag law is employed to model the bed shear stress, τ, as

$$\tau = \frac{1}{2}\rho f_c u^2 \quad . \qquad 5$$

The bedload transport is then based on the shear stress as

$$I_b = \frac{0.5\varepsilon_b \rho f_c u^2 |u|}{\tan\phi - \tan\beta} \quad (6)$$

In a like manner, the suspended load transport is

$$I_s = \frac{0.5\varepsilon_s (1-\varepsilon_b)\rho f_c u^2 |u|}{(w/U_s - (|u|/u)\tan\beta} \quad (7)$$

where φ is the friction angle associated with the sediment, ε is the load efficiency factor for the suspended (ε_s) and bedload components (ε_b), u is the instantaneous measured velocity, U_s is the suspended sediment transport velocity, and w is the sediment fall velocity.

1.3 Need for Improvement

Models derived from Bagnold's formulation are an oversimplification of the complexities of nearshore transport. His model was developed for steady, unidirectional, riverine flow. Energetics models are semi-empirical and do not resolve the details of the swash flows. As shown in equations (6) and (7), the immersed weight transport rate is related to several measured parameters and needs to be calibrated to determine a reasonable estimation of the unknown coefficients (friction factor and load efficiency).The coefficients are often calibrated with in situ data for a particular beach, but calibrating only helps get the correct order of magnitude for the transport rates and does not aid in explaining the physical processes of sediment transport (Masselink, 2001; Puleo et al., 2000).

When energetics models are applied in the swash zone, there is an offshore-directed skewness in the velocity of the swash since run-up and run-down

have similar velocity magnitudes, but the duration of the offshore-directed velocity is larger than the onshore duration. This type of formulation generally results in a net seaward transport even under accretive conditions. Many processes are not included in the model that could enhance the prediction of sediment transport in the inner surf and outer swash zone. The accuracy of the model was aided by the inclusion of a fluid-acceleration parameter. Drake and Calantoni (2001) used a discrete particle model and added a fluid acceleration term to the Bagnold equation. Assuming Euler's equation is applicable and the convective acceleration is small, the total fluid acceleration is directly proportional to the horizontal pressure gradient. With the enhanced transport equation, the model predicts a bedload efficiency an order of magnitude greater than the bedload efficiency of Bagnold (1966). This empirically-derived parameter's success at aiding sediment transport predictions has been attributed to the theory that it compensates for some of the simplifications used in deriving the quadratic stress law which governs the transport equations (Bagnold, 1966; Bowen, 1980; Bailard, 1981; Henderson et al., 2004). A secondary explanation is that under certain wave conditions, sediment mobilization is induced by a horizontal pressure gradient ($\partial p/\partial x$) applied to the seabed, instead of or in addition to the force due to vertical gradient of shear stress (Madsen, 1974;Foster et al., 2006). Pressure gradients generated by the passage of a wave can aid sediment transport.

Puleo et al. (2007) studied fluid accelerations in the swash zone using the two-dimensional numerical model NEWFLUME (Lin and Xu, 2005). They found that shoreward directed accelerations were only a small component (22%) of the swash cycle. Shoreward-directed accelerations only have the capacity to enhance shoreward transport for this short amount of time. This study enforces the results of Calantoni

and Puleo's (2006) investigation of the pressure gradient on the wave bottom boundary layer during sheet flow conditions in the surf zone. The findings from this study indicated that while $\partial p/\partial x$ is small compared with the magnitude of particle drag, the pressure gradient's peak phase aided the particle drag-induced transport by 30% in some cases.

Baldock and Hughes (2006) made field observations using the free surface slope as a proxy for the pressure gradient with an underlying assumption that the only pressure component is hydrostatic. They noted that the swash boundary layer is subjected to an adverse (opposite sign of velocity) pressure gradient during run-up and a favorable (same sign as velocity) pressure gradient during run-down. A positive pressure gradient corresponds to a water surface dipping offshore and a negative pressure gradient indicates the water surface dips shoreward. The total fluid acceleration was offshore for almost the entire swash cycle, with the exception of the region near bore collapse. The research study using the free surface slope as a proxy for the pressure gradient indicates the hydrostatic pressure gradient does not positively influence onshore sediment transport. However, that study only considered the hydrostatic pressure distribution resulting from the surface slope. The presence and magnitude of dynamic pressure gradients require further investigation. To do this, the development of a measurement technique that incorporates the total pressure under a wave needs to be developed.

Chapter 2

DEVELOPMENT OF PRESSURE MEASUREMENT TECHNIQUE

In chapter 1, the concluding remarks stated a need for new measurement techniques that are able to measure directly the total pressure near the seabed. In the following subsections, the details of such a system are explained.

2.1 Previous Measurement Techniques

Direct measurements of pressure under a wave and the subsequent calculation of the pressure gradient are not easy to obtain in the laboratory or in the field. Most pressure sensors available on the market do not measure the dynamic pressure. Several known techniques have been employed to measure and estimate the horizontal pressure gradient in the cross-shore direction of the beach.

Foster et al, (2006) characterized the pressure gradient using the acceleration of the free stream velocity. Assuming that the area of interest is in shallow water, the equation for the horizontal pressure gradient is:

$$-p_x = \rho(u_\infty)_t + \rho u_\infty (u_\infty)_x \quad , \qquad 8$$

where subscripts denote differentiation with respect to the subscripted variable, u_∞ is the free-stream wave velocity. An approximation of the pressure gradient using linear wave theory yields (assuming the convective accelerations are small)

$$-p_x = \rho(u_\infty)_t \qquad 9$$

From equation (9), a non-dimensional parameter, the Sleath parameter (Sleath, 1999) was created as an indicator for the formation of plug flow. Plug flow is described by sediment moving as a solid block *(plug)* during flow reversal in an oscillatory flow. In a more general sense, the Sleath parameter can be used as an indication of sediment mobilization during a wave cycle. Currently, the flow reversal of interest is the change from offshore to onshore, because that is the phase where pressure gradients could have a contribution to onshore sediment transport. The parameter is shown in equation (10) with the approximation using (9) given in equation (11)

$$S(t) = \frac{\rho u_{\infty_t}}{(\rho_s - \rho)g}, \qquad 10$$

where ρ_s is the sediment density.

$$S(t) = \frac{-p_x(t)}{(\rho_s - \rho)g} \qquad 11$$

Using the incorporation of Equation (10) as an approximation for measuring the pressure gradient, the first field evidence of pressure gradient induced

sediment motion was recorded in a study on surf zone sand bar migration (Foster et al., 2006). They found, from observations of velocity and sediment that under large pressure gradients during onshore-directed flow, several centimeters of sediment were mobilized and transported onshore.

As mentioned in Chapter 1, Baldock and Hughes (2006) used the slope of the free surface as a proxy for measuring the pressure gradient in the swash zone. Using a series of horizontal string lines starting at the beach face, the direction of the slope of the incident wave can easily be determined by images taken of waves passing over the horizontal datum. With this technique, the results are contradictory to the results of Foster et al. (2006) that showed the horizontal pressure gradient could aid onshore transport.

Another technique to measure the pressure gradient on a beach face is by installing a series of gauge pressure transducers along the beach face (Figure 2.1).

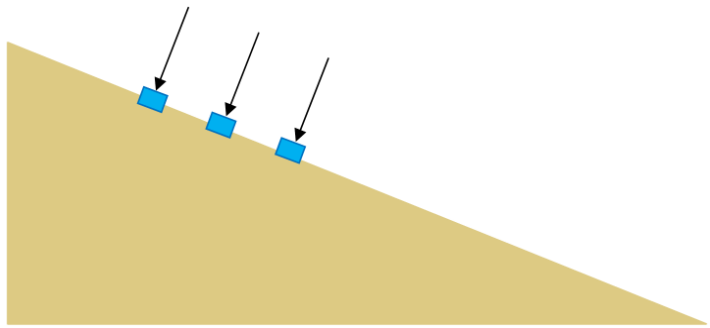

Figure 2.1: Schematic of simple pressure transducers deployed on a beach face.

Most pressure transducers are only capable of detecting pressure normal to their surfaces. In the above figure, each sensor is capable of detecting pressure normal to the beach face following direction of the arrows. This setup is similar to the one used in the laboratory experiments of Suzuki et al., (2010). Such a design might provide insight into the pressure of a wave breaking on a steep slope where the majority of the flow is normal to the beach face and the only concern is the actual force of the breaking wave. For flows following the breaking of a wave, a pressure measurement system that accounts for the bed-parallel difference in pressure is more ideal.

2.2 Design Considerations

The ideal pressure sensor to measure the total pressure in the inner surf and outer swash zone should be able measure both the hydrostatic pressure due to the water level, as well as the bed-parallel dynamic pressure. The sensor must be fully submersible and small enough so that its size does not greatly alter the flow field. Ideally, the sensor should be able to work, even after it is alternately covered and uncovered by passing waves in the swash zone.

2.3 Working Design

Several possible designs have been considered. Ultimately, the chosen design for the pressure sensor apparatus is based on the use of simple gauge pressure

transducers, but with several modifications to their traditional setup. The selected pressure transducer is the PX26-001GV from OMEGA. This transducer has a range of 0-1 PSID (Pounds per Square Inch Differential). Figure 2.2 shows the relative size of the pressure transducer. The small size of this particular transducer makes it ideal for deployment in the inner surf and swash zone.

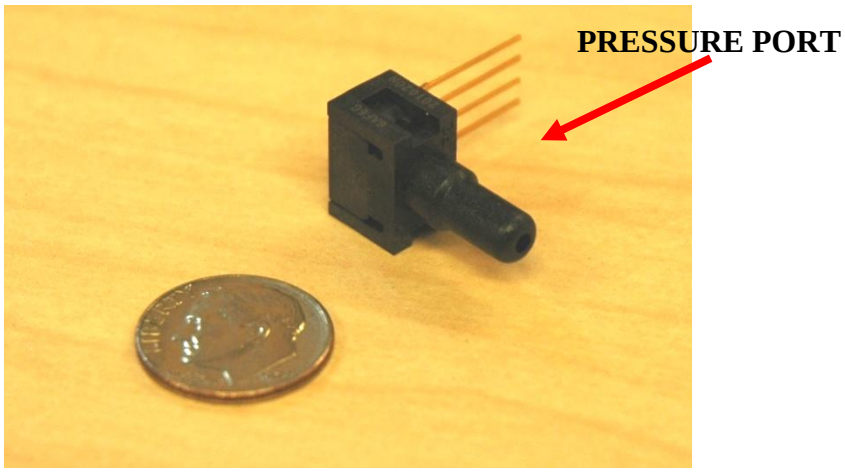

Figure 2.2: The simple gauge pressure sensor transducer is has a very small sampling area. This feature makes it a good product to use in nearbed and nearshore measurements.

Figure 2.2 also points out the pressure port location on the transducer. A continuous fluid from the measurement position to the transducer enables the transducer to detect small changes in pressure at bed-level. The pressure port in the transducer was filled with water using a small syringe. Flexible Tygon tubing and plastic reducer coupling devices were used to connect the transducer to a hollow aluminum rod. The rod is affixed to the bed of the wave flume with the opening of the pressure port at bed-level

and bed-parallel. The hollow aluminum rod has an outer diameter of 2.38mm. This small opening makes the rod a good choice of pressure sensor due to the minimal disruption in wave flow patterns and the ability to place several of the pressure ports in a tightly-spaced array for the calculation of pressure gradients over a narrow cross-shore distance.

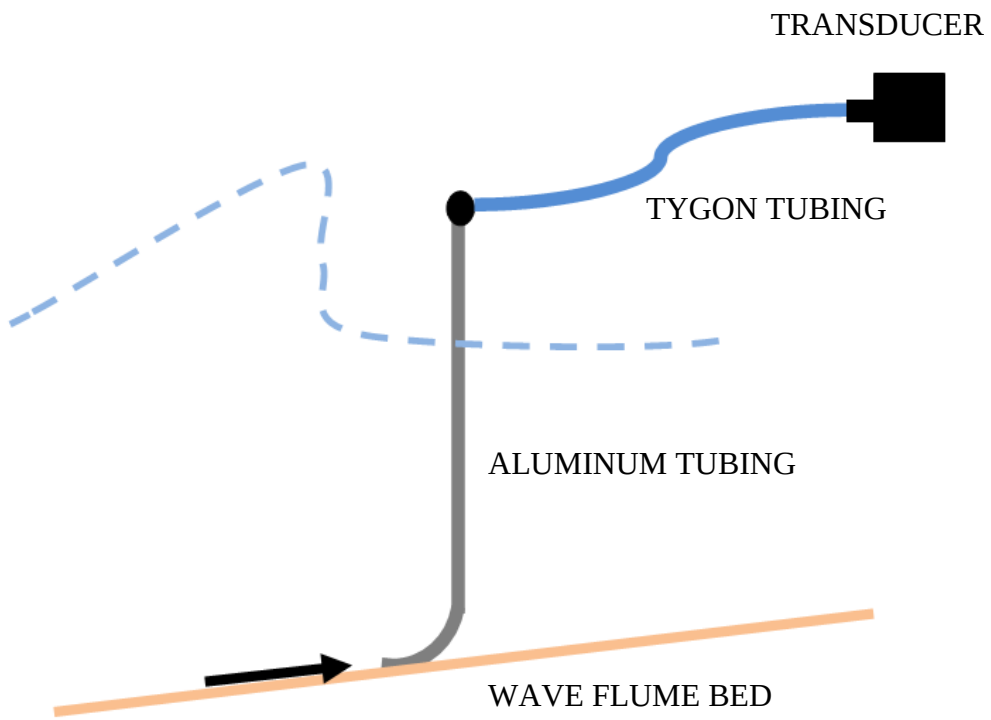

Figure 2.3: This schematic shows a pressure sensor deployed in the inner surf zone with aluminum pressure port parallel to the sea bed

To calculate the total and dynamic pressure at multiple locations, an array of pressure transducers was used. The solution is the manifold shown in Figure 2.4 and the aluminum pressure port array in Figure 2.5. The 8 pressure ports will allow for the measurement of the total pressure during both onshore-directed and offshore-directed wave motion by including the dynamic pressure under the wave.

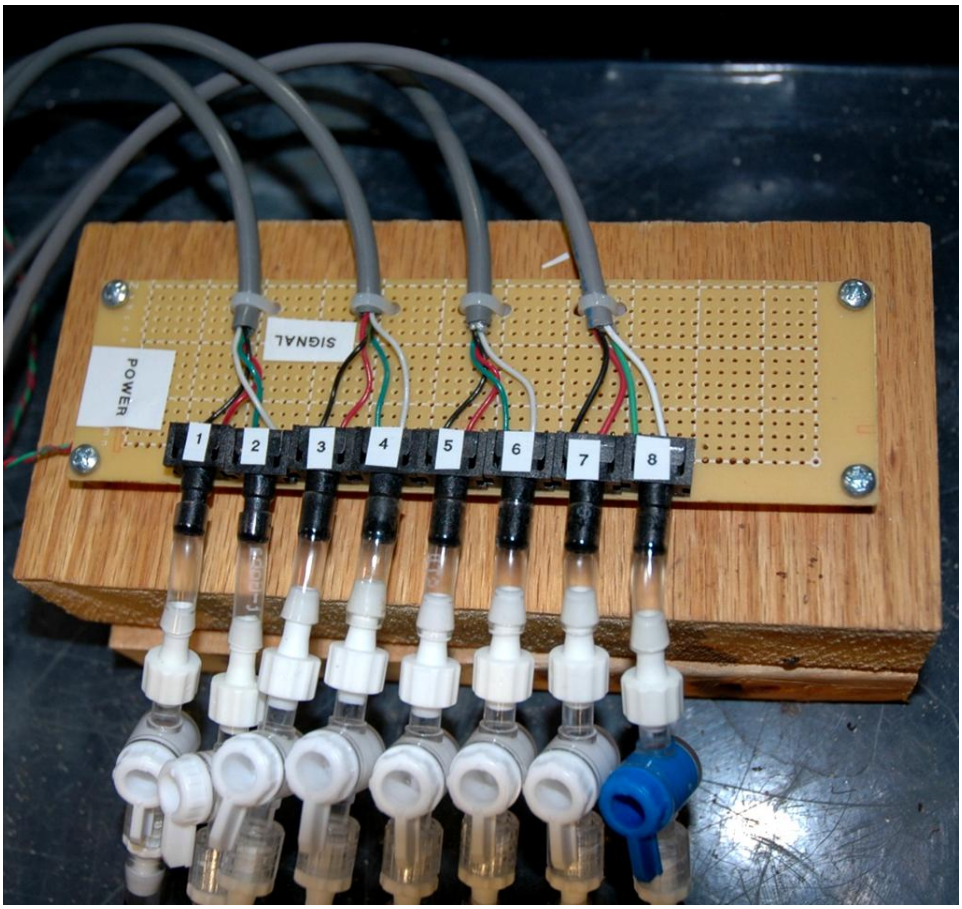

Figure 2.4: This manifold is the connection between the measurement system of pressure transducers and the data-logging system. The pressure transducers are shown connected to the water-filled Tygon tubing.

The 8 aluminum pressure ports are arrayed along the beach face in pairs. Each pair of pressure sensors has one offshore-directed and one onshore-directed port. The pressure port pairs are co-aligned in the cross-shore direction (See Figure 2.5).

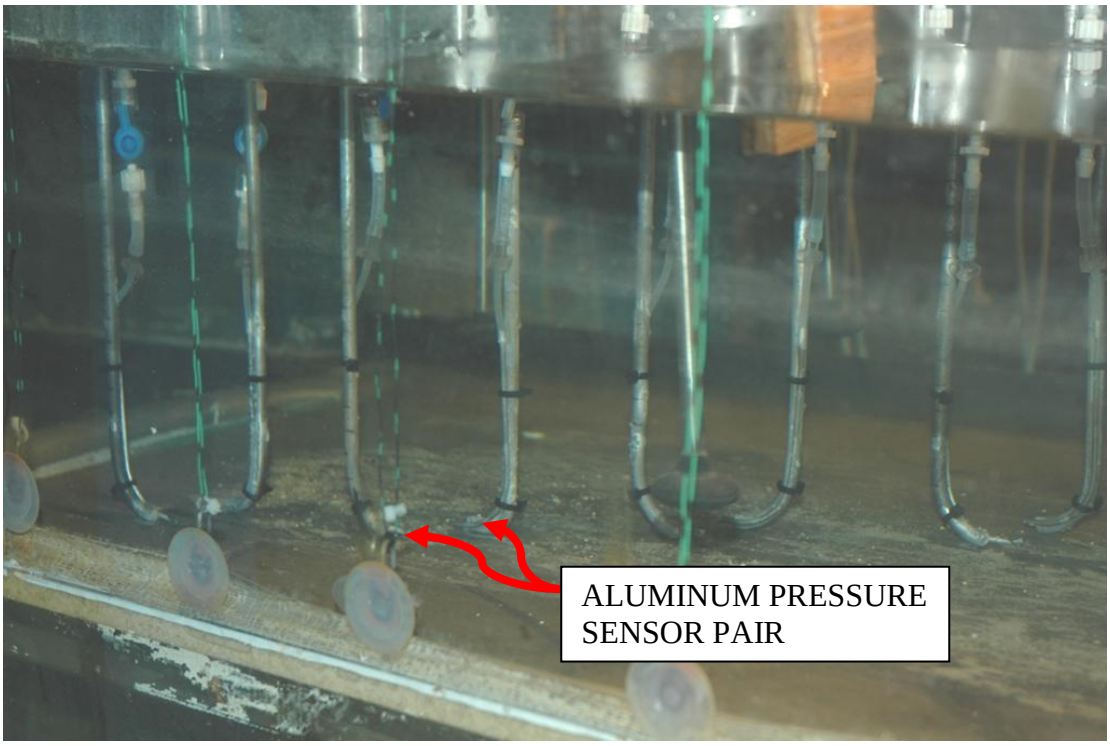

Figure 2.5: Aluminum pressure ports are shown deployed in the inner surf zone of the wave flume.

For each pressure sensor pair, the pressure signal for the onshore-facing sensor and offshore-facing sensor were combined to one signal as determined by the direction of the flow in the wave flume (Figure 2.6). When the flow is onshore-directed, the pressure signal is positive and a negative sign is associated with an offshore-directed flow. Therefore at the zero-crossings of the pressure signal, the combined signal switches pressure ports, because only one of the sensors in a pair has the capacity to capture the hydrostatic and dynamic pressure.

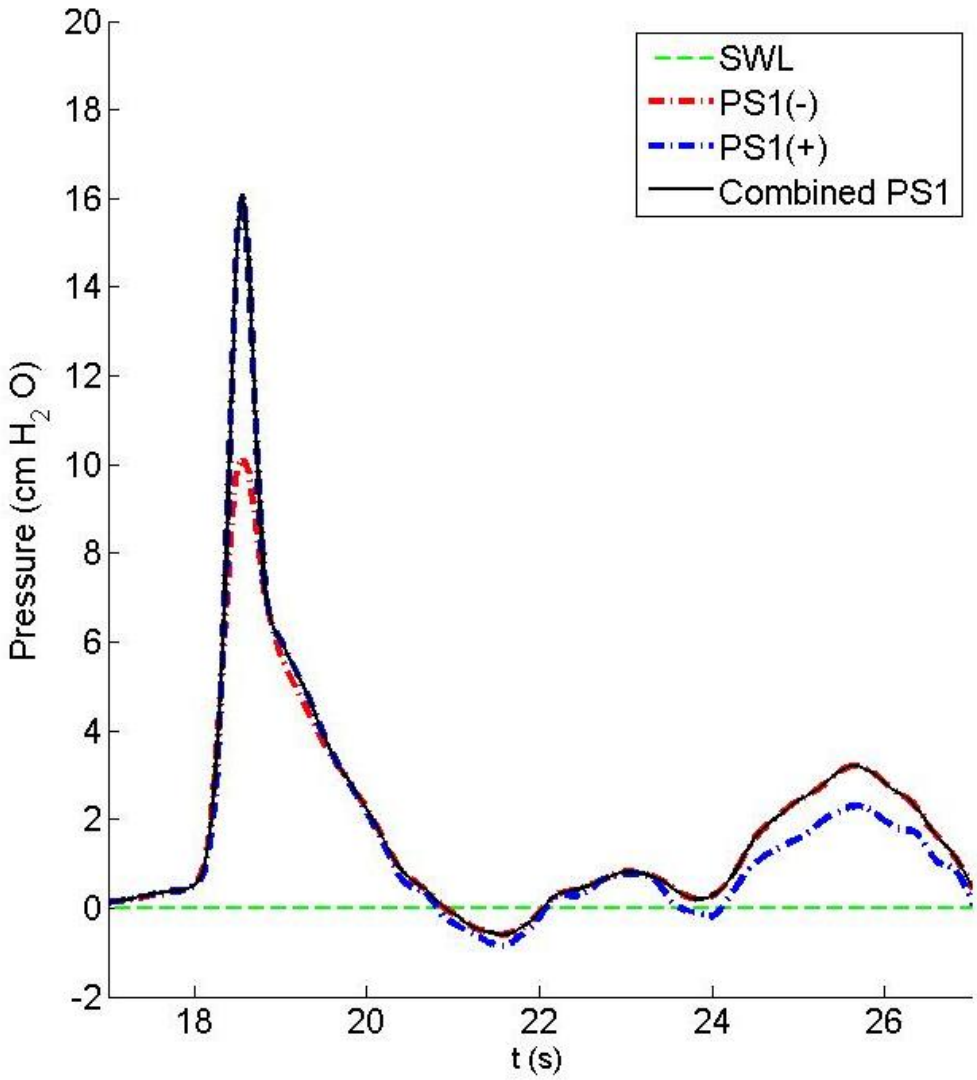

Figure 2.6: The "total pressure" time series is derived from combining the signal from each onshore-offshore sensor pair.

Using the combined pressure signal from each of the four pressure sensor pairs, three total horizontal pressure gradients were derived across the 0.01 m cross-shore spacings of the sensor pairs.

Chapter 3

EXPERIMENTAL DESIGN AND SETUP

To do a thorough experimentation of any nearbed measurements in the inner surf and outer swash zone, it would be idyllic to test and use the instrumentation on an actual beach under the various wave conditions that occur there. However, for the development of a new pressure measurement technique, the measurement system is first tested with a rigorous series of laboratory experiments in a wave flume using idealized conditions. While the simplified conditions of a wave flume remove important processes, the well-controlled laboratory environment allows for the repeatability and ease of analysis needed to initially test the pressure gradient measurement system. Figure 3.1 shows the ideal progression of the experimental process. Due to limitations of the wave flume, the monochromatic wave and irregular waves are incomplete.

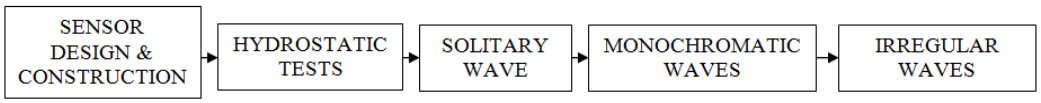

Figure 3.1: A flow chart of the pressure gradient laboratory experiment shows the different experimental test cases.

Although the reasoning behind the pressure measurement system was discussed in Chapter 2, the overall experimental setup and calibration are detailed in the following subsections.

3.1 Precision Wave Flume

All experiments were conducted in University of Delaware's Center for Applied Coastal Research using the Precision Wave Flume. The wave flume has a total length of 33 m, but the entire length of the tank was not utilized due to the construction of a vertical wall 22.6m from the wave paddle. The dimensions for this series of experiments are shown in Figure 3.2. The 1:12 sand beach is in place due to another series of experiments running concurrently with the horizontal pressure gradient experiments.

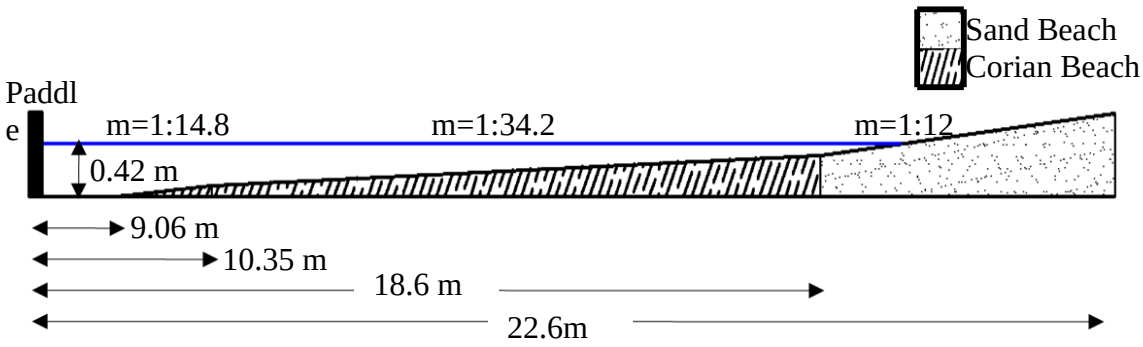

Figure 3.2: The dimensions of the Precision Wave Flume at the Center for Applied Coastal Research are shown above. All units are in meters unless otherwise noted. The 1:14.8 slope and the 1:34.2 slope are solid surfaces and the 1:12 slope is a sandy beach.

3.2 Wave Generation

The waves for this experiment were generated using a piston-type wave paddle at the offshore limit of the wave flume. The water depth at the paddle was 0.42 *m*. The waves were generated using a 90 second time series of voltages read by the wave maker at 50 *Hz*. The voltage values in the time series are associated with different paddle displacements that result in the desired wave motion. In this case, the wave motion was a solitary wave. In the initial testing of the pressure sensors, it was desirous to use a simple wave forcing. The selected wave type was a solitary wave since this wave type meets the basic criteria:

- Sufficient strength to cause sediment transport in the inner surf and outer swash zone.
- Does not exceed the run-up limit of the wave flume as determined by a vertical wall 22.6 *m* from the offshore wave paddle.
- Simple wave type that allows for easy analysis of nearshore processes.

3.3 Instrument Array and Calibration

The experimental setup requires the use three different measurement devices: pressure sensors, electromagnetic current meters, and capacitance wave gauges. The development and implementation of the pressure sensors were detailed in Chapter 2. The following subsections show how the three sensors work in conjunction, their relative placement in the wave flume, and their calibration methods. Figure 3.3

gives an overview of the instrumentation. All of electromagnetic current meters, capacitance wave gauges, and pressure sensors were connected to National Instruments data logger and recorded at a rate of 16 Hz and analyzed in Labview programming environment. The sampling rate was limited by the highest sampling rate of the EMCMs, which was 16 Hz.

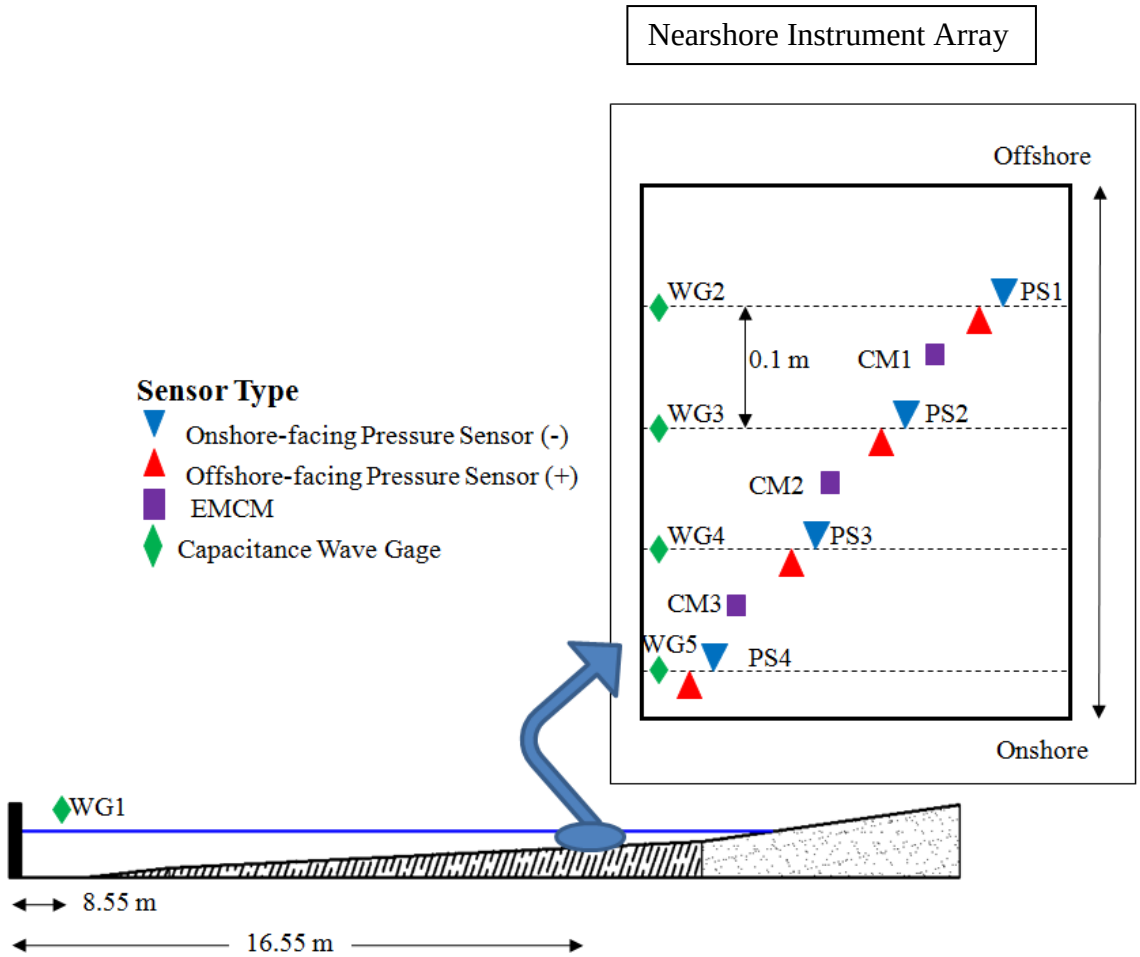

Figure 3.3: The elevation of the wave flume is shown with an inset enlargement of the location of the various sensors used in this experiment. WG is used to reference the capacitance wave gauges, PS will denote the pressure sensors and CM refers to the electromagnetic current meters. The array of sensors begins at 16.55m from the wave maker paddle with the exception of the WG1, the offshore wave gauge that is located 8.55 m from the wave maker paddle.

3.3.1 Capacitance Wave Gauges

Five wave gauges were used in the experiment and the locations of each gauge in the wave flume and a description are shown in Table 3.1, as well as the R-square values for each sensor's calibration.Each distance is measured from the offshore wave maker paddle.

Table 3.1: Wave gauge cross-shore locations

WG	*x* [m]	R-square Value	Type
1	8.55	0.9988	Carriage-mounted
2	16.55	0.9988	Wall-mounted
3	16.65	0.9986	Wall-mounted
4	16.75	0.9980	Wall-mounted
5	16.85	0.9985	Wall-mounted

Two different models of wave gauges were utilized in this experiment. The first type, the carriage mounted wave gauge, was used offshore (WG1). The four wave gauges located within the nearshore instrument array use a wire held against the wave flume wall using a set of suction cups. Both types rely on the same usage of measuring the voltage change in the immersed wire as each wave passes. Some concern existed due to the proximity of WG2-5 to the wave flume wall. This issue was addressed and the wall effect is on the order of 1mm (Hicks et al., 2010). All of the wave gauges were calibrated by manually changing the water level in 0.1m increments. For each water

level, voltage was recorded for 15 seconds. A linear fit was applied to series of mean voltages and water levels for each sensor. The linear fit relationship between the water level and the voltages had R^2 values very close to 1.0 as shown in Table 3.1, meaning that the fit provided a robust representation of the calibration measurements.

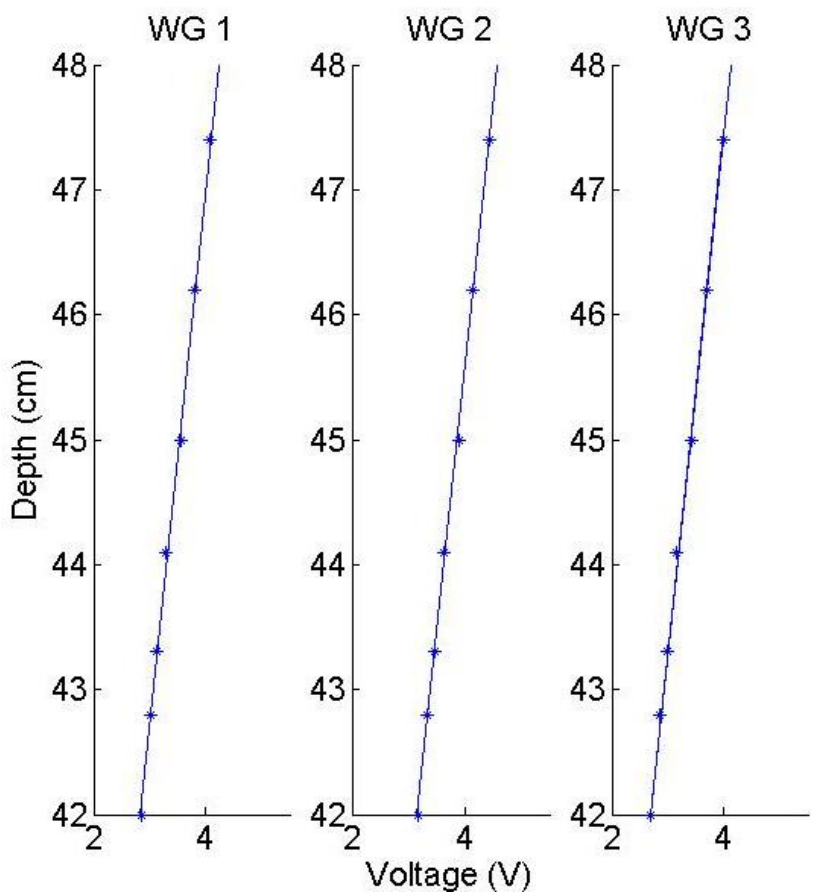

Figure 3.4: The calibration curve showing the linear fit for three different wave gauges. WG1 is the offshore wave gauge mounted on a carriage. WG 2 and 3 are a part of the Nearshore Instrument Array.

3.3.2 Electromagnetic Current Meters

Three electromagnetic current meters (CM) were positioned with 0.1 m cross-shore spacing and 0.03 m from the bed in the Nearshore Instrument Array. CM1, CM2, and CM3 were positioned halfway between the sensor pairs as shown in Table 3.2. The current meters measure how quickly the water moves past the sampling volume of water. The current meters have the capacity to measure fluid velocity in 2 directions, but only the cross-shore (x) direction was collected and used in this experiment.

Table 3.2: CM1, CM2, and CM3, are evenly spaced in the cross-shore direction. z_b denotes the distance from the bed of the flume to the sampling volume of the current meter.

CM	x	z_b
	[m]	[cm]
1	16.60	3
2	16.70	3
3	16.80	3

With this placement, at each point where $\partial p/\partial x$ is calculated, the instantaneous nearbed velocity is also known, and the acceleration can be calculated.The current meters require no in-situ calibration and directly output velocity in units of m/s to the data logger.

3.3.3 Pressure Sensors

The eight pressure sensors were calibrated using the same technique as the wave gauges. The calibration curves for each sensor were determined and applied to each data set. The pressure posed an occasional challenge as a direct result from the

water-filled Tygon Tubing. If small air bubbles accumulated in the tubing, a discontinuity in the fluid was introduced and the pressure signal became unreliable. To ensure that the first set of experiments involving this pressure measurement technique had minimal technical errors, the Nearshore Instrument Array was placed in the surf zone, so that the pressure sensor apertures stay fully submerged for each wave cycle. The tubing required regular cleaning and maintenance to ensure a linear calibration curve and accurate measurements. The pressure pair locations and R-square values for the calibration curves are shown in Table 3.3 and the calibration curves for pressure sensors PS1, PS2, and PS3 are identified in Figure 3.5.

Table 3.3: Each pair of pressure sensors is co-located with one of the wall-mounted wave gauges in the Nearshore Instrument Array.

PS	*x* [m]	R-square Value	Co-located WG
1(-)	16.55	0.9986	WG2
1(+)	16.55	0.9985	
2(-)	16.65	0.9986	WG3
2(+)	16.65	0.9892	
3(-)	16.75	0.9985	WG4
3(+)	16.75	0.9985	
4(-)	16.85	0.9987	WG5
4(+)	16.85	0.9985	

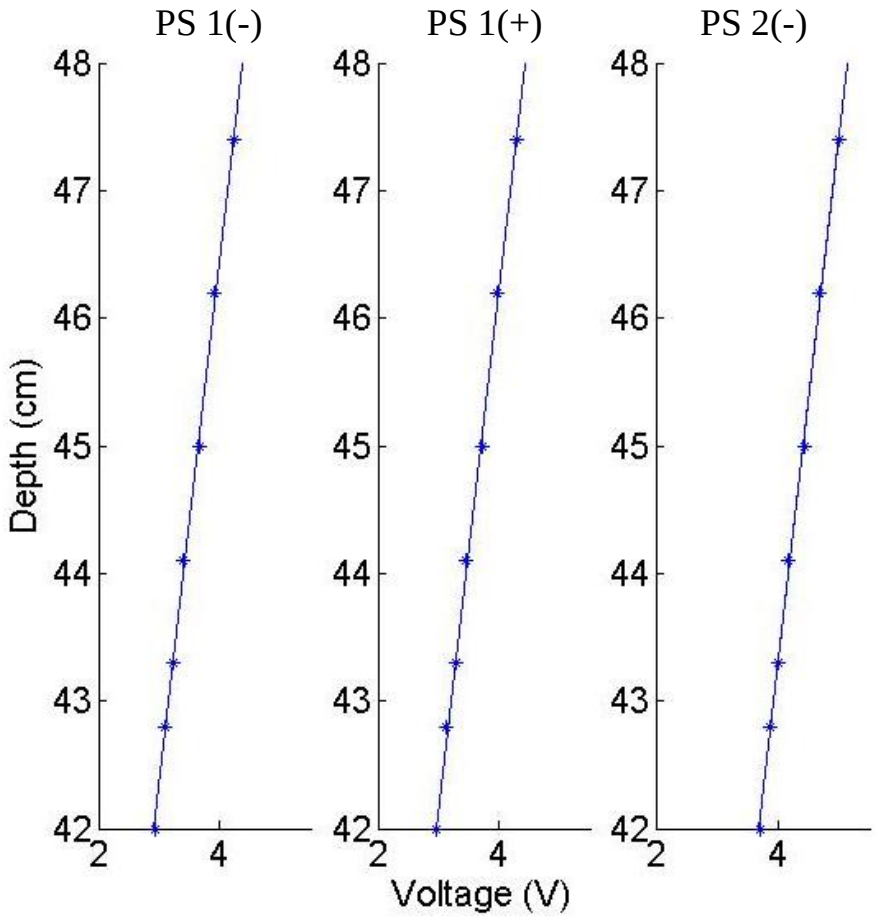

Figure 3.5: The Calibration curves for three different pressure sensors show the linear fit relationship between the pressure and voltage.

Chapter 4

EXPERIMENTAL RESULTS

4.1 Output

Initially, the three tests shown in Table 4.1 were all to be analyzed and discussed. Table 4.1 shows the three experimental test cases are detailed. *H* represents the significant wave height. *T* is the wave period. n_w is the number of waves in each test run and n_t is the number of tests that were ensemble averaged.

Table 4.1: Experimental Test Cases

CASE	Wave Type	H (m)	T (s)	n_w	n_t	Status
01	Solitary	0.15	--	1	10	Complete
02	Regular	0.18	2.5	8	6	Future Work
03	Irregular	--	--	--	--	Future Work

Out of the three different wave types, only Case 01, the solitary wave, will be used due to the set up of a low frequency oscillation in the wave flume that caused irregularities in the pressure sensor readings for Case 02 and Case 03 (Figure 4.1).

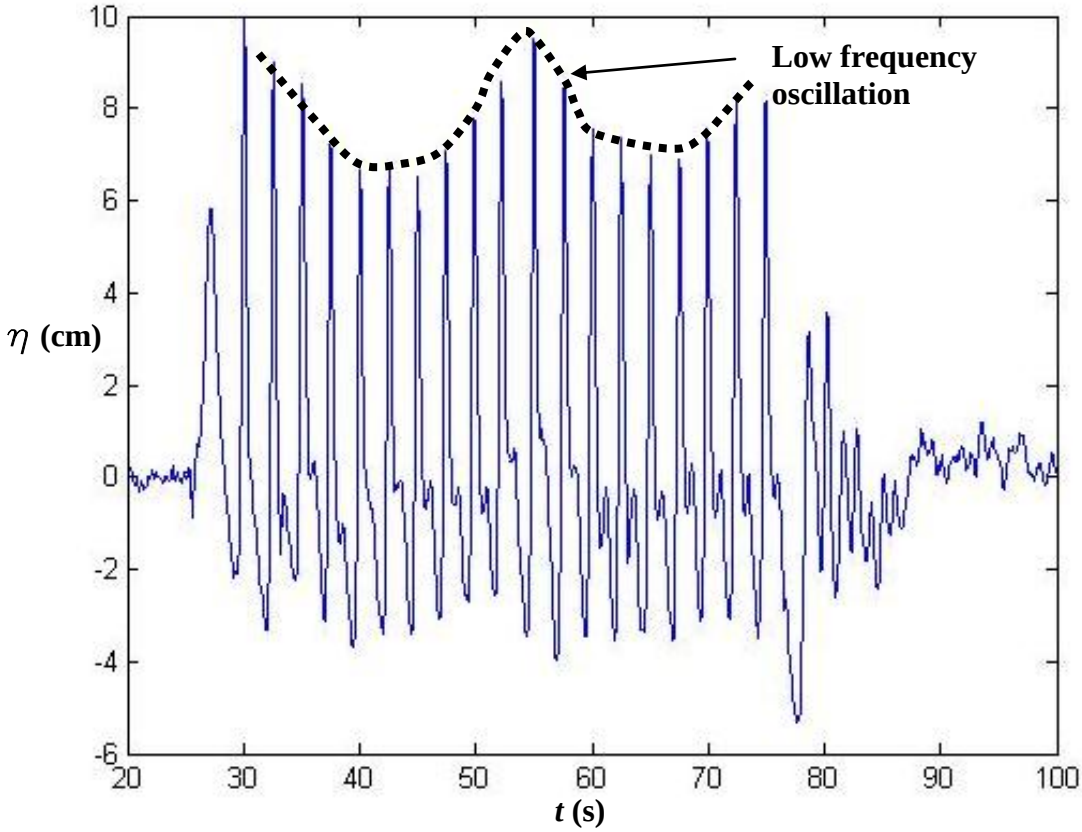

Figure 4.1: The low frequency oscillation in the Precision Wave Flume is evident in this long time series of surface fluctuations for 20 monochromatic short waves at location WG1.

For Case 01, the raw outputs from the data logger were the free surface, the pressure and the velocity, from the wave gauges, pressure sensors, and current meters, respectively. For Case 01, 10 tests were completed and the time series were calibrated using the methods mentioned in Chapter 3 and the calibrated data were ensemble-averaged.

4.1.1 Free Surface

The solitary wave height is shown (Figure 4.2) in terms of the fluctuation of the free surface. A zero value denotes a still water level of 0.42 m.

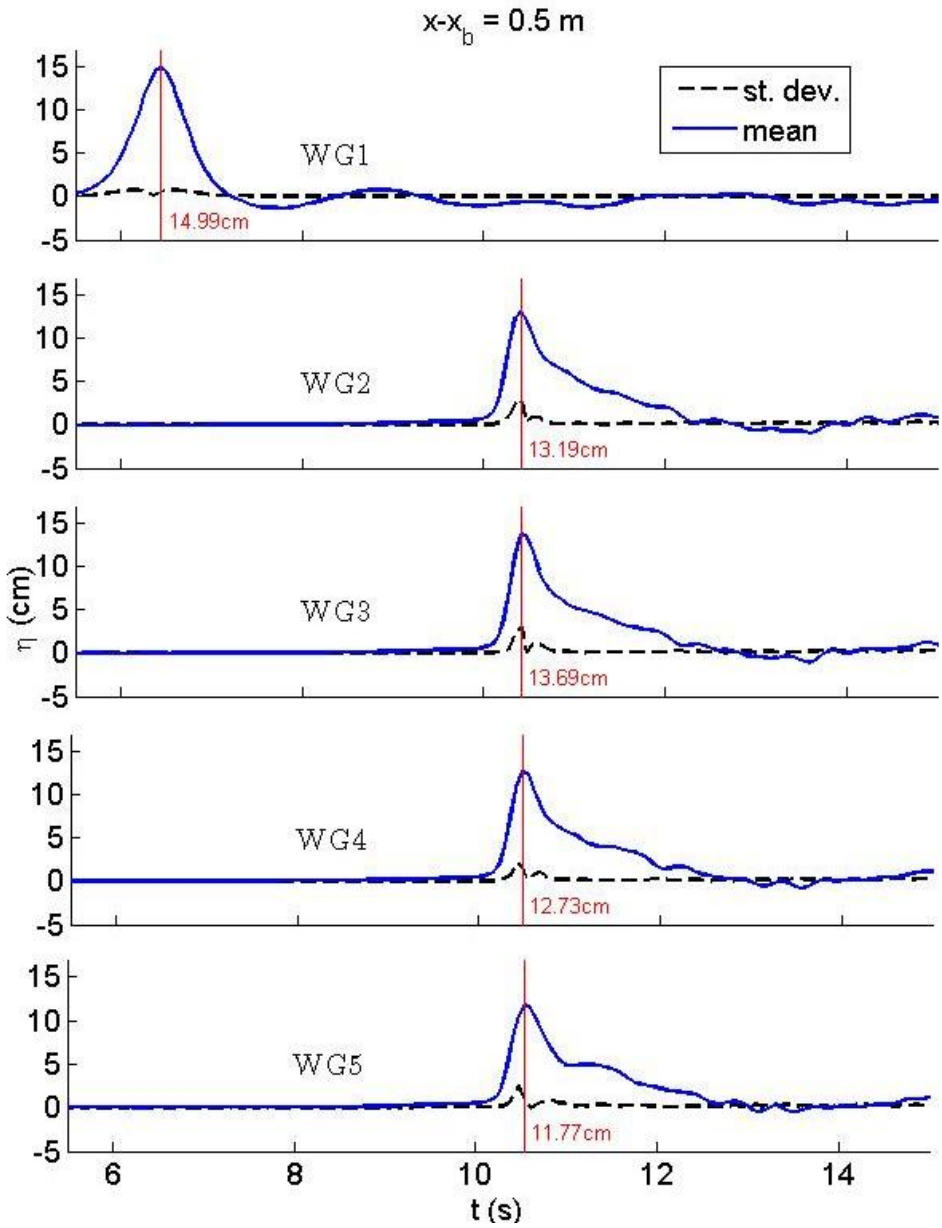

Figure 4.2: The ensemble average of the free surface fluctuations at each WG location. The black dashed line denotes the standard deviation, and the red vertical line is the average peak wave height

The unbroken wave is shown at the WG1 location; all subsequent frames are after breaking and in the inner surf zone (WG2-5). At WG1 the unbroken wave height is 0.15m. After breaking and towards the landward edge of the inner surf zone, the wave has an ensemble-average height of 0.12 m.

4.1.2 Pressure

The ensemble average for each pressure sensor location is shown in Figure 4.3. The units of pressure for the sensors are presented in *cm* to make simple comparisons to the change in the free surface as shown in Equation (12).

$$\text{Relative depth (cm)} = \frac{P}{\rho g} \qquad 12$$

As the solitary wave passes over each sensor pair (Figure 4.3), the peak in pressure is different for the onshore and offshore facing sensors.

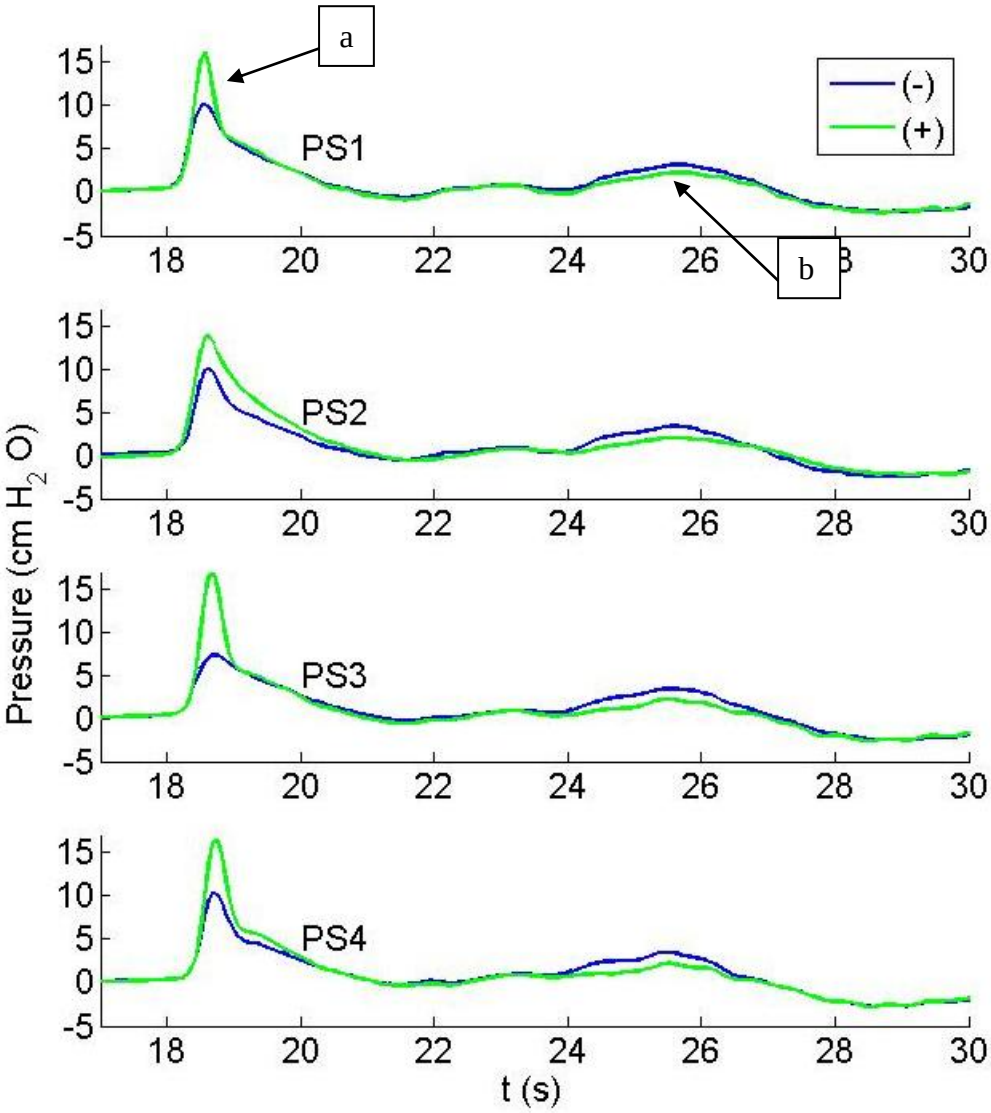

Figure 4.3: The ensemble average of 10 waves for each pressure sensor (PS1-PS4). Each pressure sensor pair is on the same subplot. (-) is shoreward facing and (+) is offshore facing

The (-) pressure sensors are shoreward facing and capture the offshore-directed total pressure during flow reversal. The (+) pressure sensors are offshore-facing and capture the onshore total pressure during run-up. The “a” marker shows the initial wave passing over PS1, 16.55 m from the wave paddle. The “b” marker shows the reflected wave returning offshore towards the wave paddle. At point “a”, $PS1_{(+)}$has a larger reading than $PS1_{(-)}$ (onshore facing sensor), and this trend is reversed at point “b’’. The same trend is shown at the three subsequent pressure sensor pairs in the figure.

Point “a” is highlighted when the sensors pair’s time series are shown focusing only on the solitary wave motion in Figure 4.4.

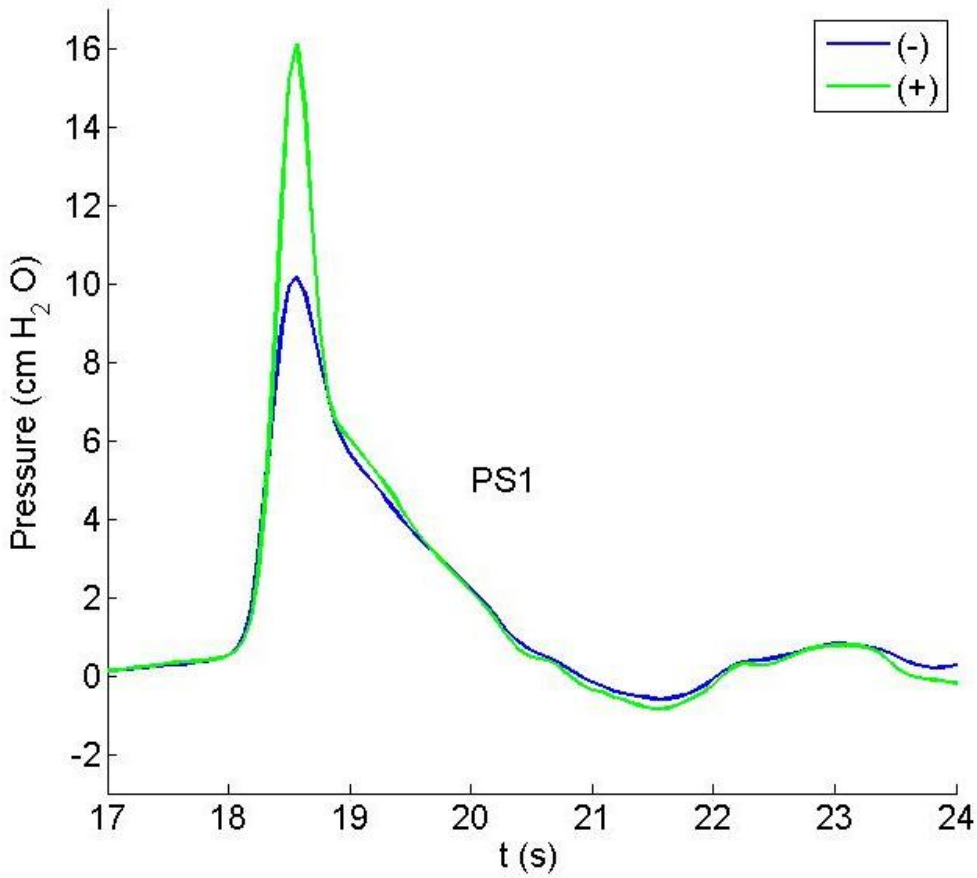

Figure 4.4: The shoreward-facing sensor (PS1) shows a distinctly smaller value of maximum pressure head than the offshore-facing sensor (PS2).

In terms of head, $PS1_{(+)}$has a maximum value of 16.11 cm at the peak of the solitary wave. $PS1_{(-)}$ has a maximum value of 10.17 cm at the peak of the solitary wave at the same cross-shore location. This difference is the basis for the computation and analysis of the dynamic pressure gradient to be discussed later in this chapter and lends credence to the hypothesis that the hydrostatic pressure is not an acceptable substitute for a measurement of the total pressure.

4.1.3 Velocity

The next key elements in the data collection are velocity data (Figure 4.5). The three ensemble-averaged cross-shore velocity time series are shown below.

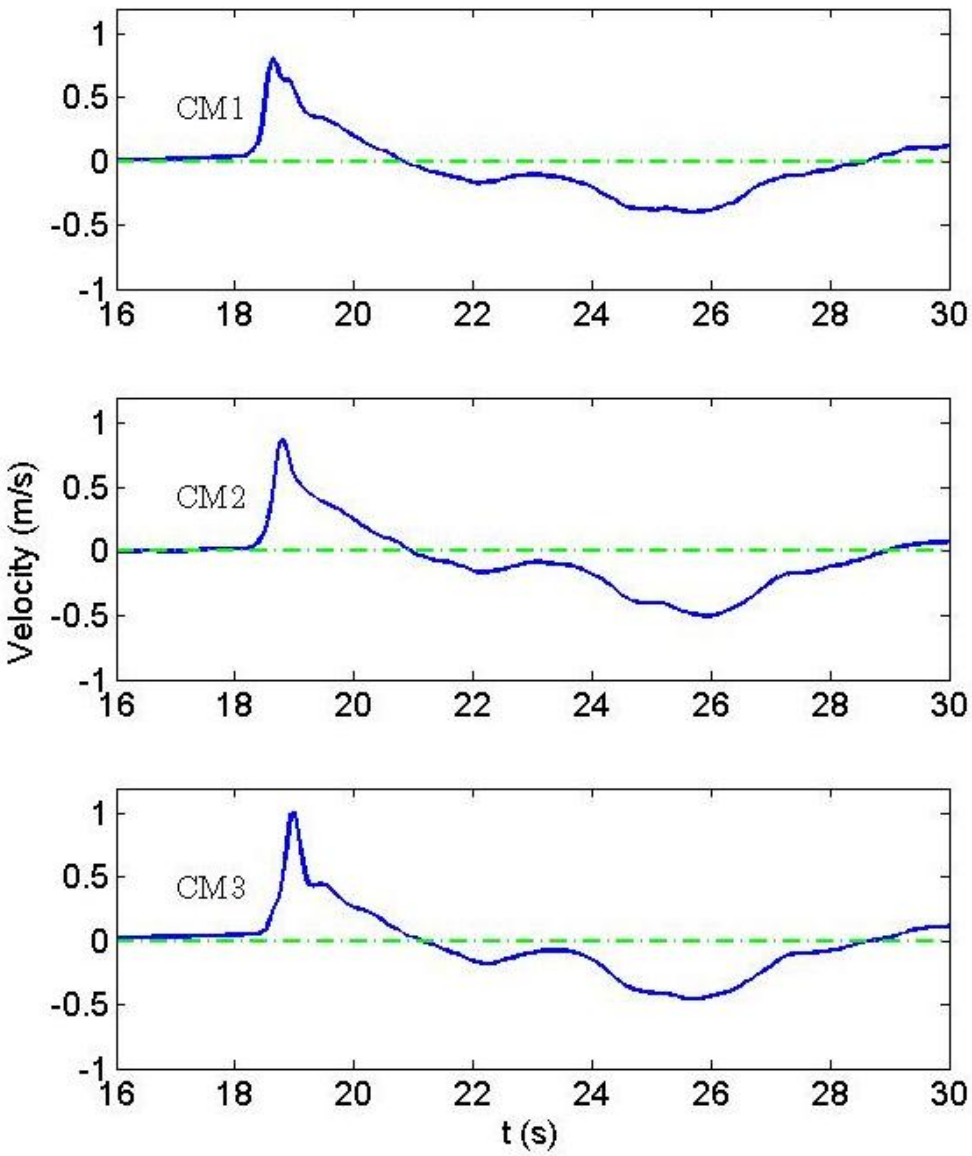

Figure 4.5: The cross-shore velocity time series for CM1, CM2 and CM3 are shown. A positive value denotes an onshore-directed velocity.

A positive cross-shore velocity means the fluid is moving in the onshore direction, and a negative value denotes the return flow propagating offshore again. The maximum onshore velocity is 1.01 m/s at CM 3. The maximum velocity varies by 0.20 m/s over the 20 cm distance between CM1 and CM3. The velocity at each location (CM 1-3) is used in the subsequent pressure gradient analysis.

4.2 Pressure Gradient Analysis

The total pressure at each pressure sensor location was determined by combining the signal from each onshore- and offshore-facing pair using the zero-up-crossing method. The hydrostatic pressure at each of the four locations was simply the wave gauge output. The still water level (SWL) was subtracted from the signal, so a value of zero denotes the still water line, and not zero pressure.

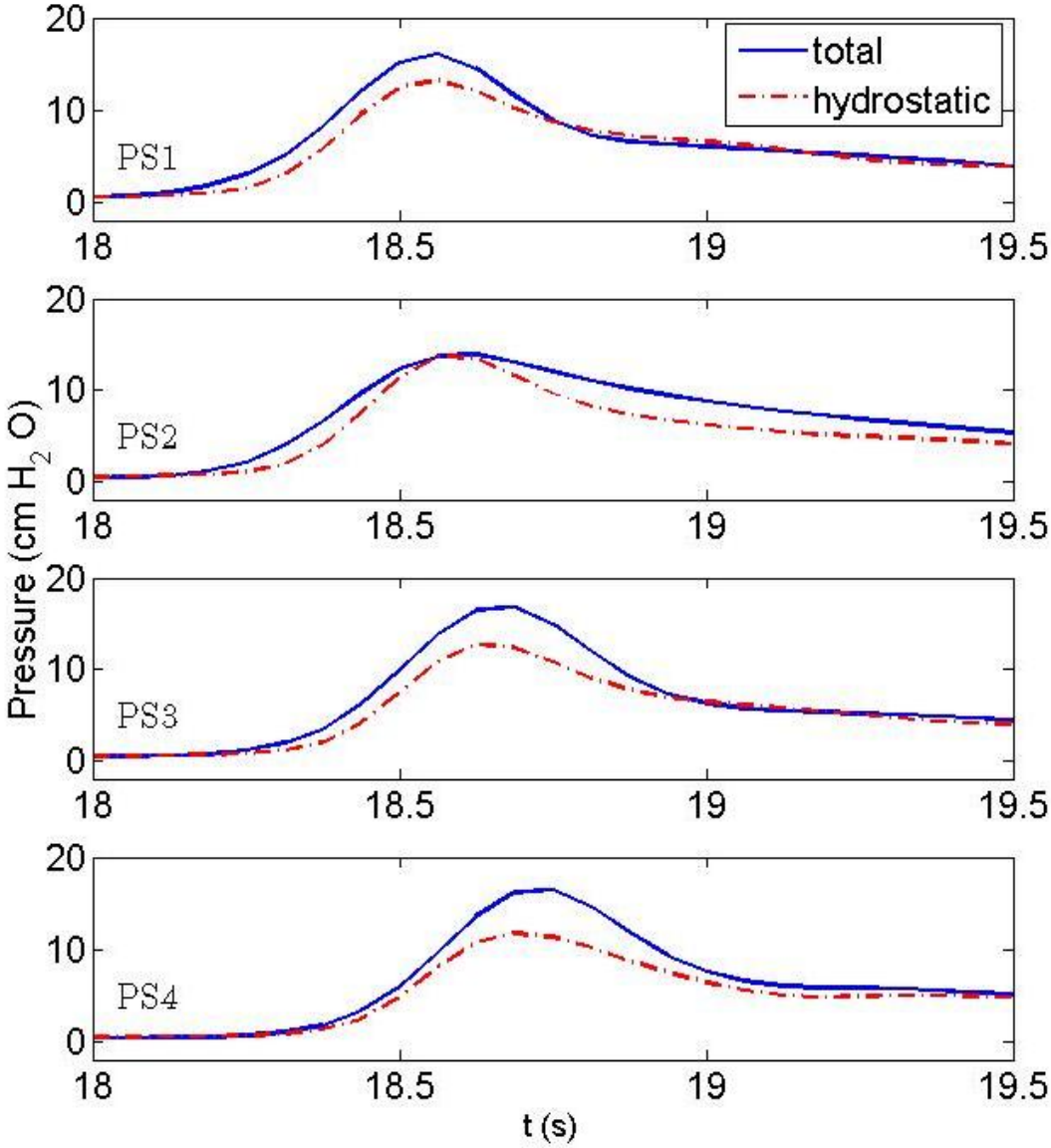

Figure 4.6: The total pressure time series derived from each sensor pair, and the hydrostatic pressure times series (from each co-located wave gauge) are shown over the 1.5 second time span during which the wave crest passes the Nearshore Instrument Array.

In three out of four locations, there is a noticeable difference in the pressure magnitude between the total pressure and the hydrostatic pressure (Figure 4.6) as the crest of the broken wave passes over the sensor location. The difference between measuring the total pressure or just the hydrostatic pressure can vary up to 28.4% at the crest of the wave and by even larger percentages slightly preceding the wave crest, according to the total and hydrostatic time series (Figure 4.6 PS4). The dynamic pressure at each location can be obtained by subtracting the hydrostatic pressure from the total pressure (Figure 4.6). For a large majority of the onshore-directed wave motion, the dynamic pressure is a large component of the total pressure.

For insight into the horizontal pressure gradient under this solitary wave, the pressure gradient is converted into a non-dimensional value

$$S(t)_P = -\frac{dp}{dx}\frac{1}{\rho g}, \qquad 13$$

allowing for comparison between the pressure gradient and the acceleration. The non-dimensional pressure gradient will be referred as $S(t)_p$ and the non-dimensional acceleration is $S(t)_a$. Figure 4.7 shows non-dimensional total and hydrostatic horizontal pressure gradients for the three 10 cm spacings between the pressure sensor pairs using a first order differencing scheme.

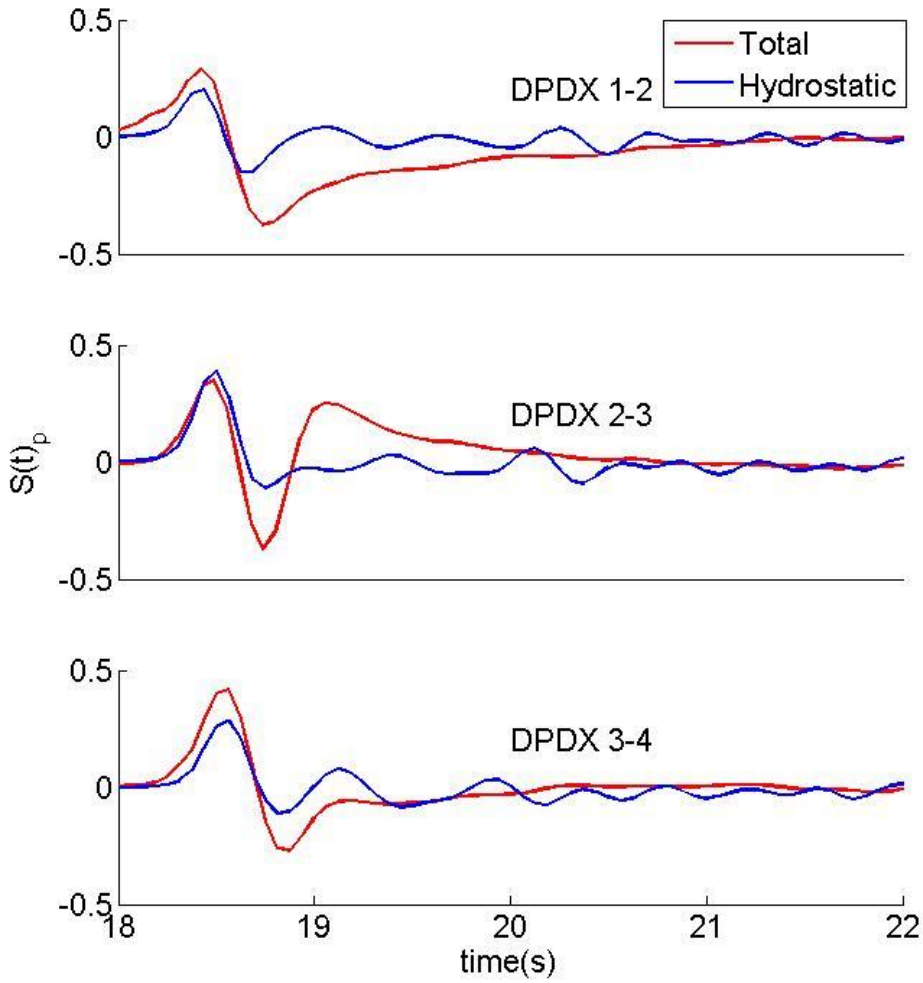

Figure 4.7: The total and hydrostatic pressure gradients are shown in non-dimensional form

The pressure gradient time series (Figure 4.7) show the difference between measuring the pressure gradient by assuming an entirely hydrostatic pressure and by including the dynamic pressure. Each pressure gradient is over a 10 cm cross section of the

flume and the numbers correlate to which pressure sensor pairs each pressure gradient was derived from. DPDX 1-2 and 3-4exhibit the same trend of a larger total pressure peak as the wave passes over the sensors. DPDX 2-3 has the anomaly of the wave gauge derived hydrostatic pressure gradient having a larger magnitude than the total pressure. The reason for this could be a result of measurement error due to small air infiltration into the Tygon tubing of PS2. A reference to Figure 4.6 shows that the DPDX 2-3 just carries through the anomaly of PS2.

Since the quality of PS2 is called into question in this data set, a different method of calculating the pressure gradient is pursued.

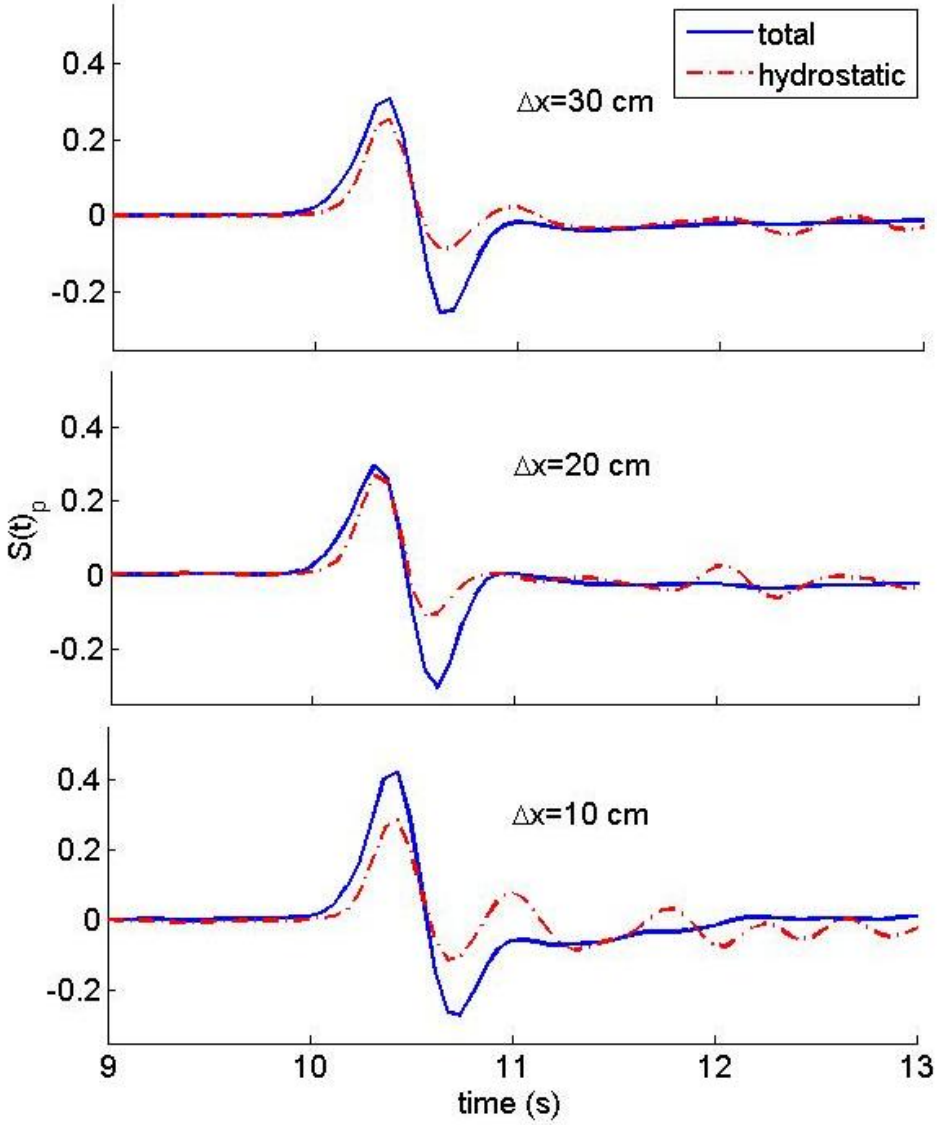

Figure 4.8: The total and hydrostatic pressure time series are calculated across three different Δx values of 30 (PS1 to PS4), 20 (PS1 to PS3), and 10 cm (PS3 to PS4).

In this second method, the pressure gradient is calculated between PS1 and PS4, across the 30 cm cross-shore span between the two sensor locations. Here, 17.64% of the total pressure cannot be accounted for by using the hydrostatic pressure as a proxy for the total pressure, and is a result of the dynamic pressure gradient.

The acceleration at each CM location was found using a central differencing scheme. The results, along with the corresponding velocity signals and non-dimensionalized pressure gradient are shown in Figure 4.9.

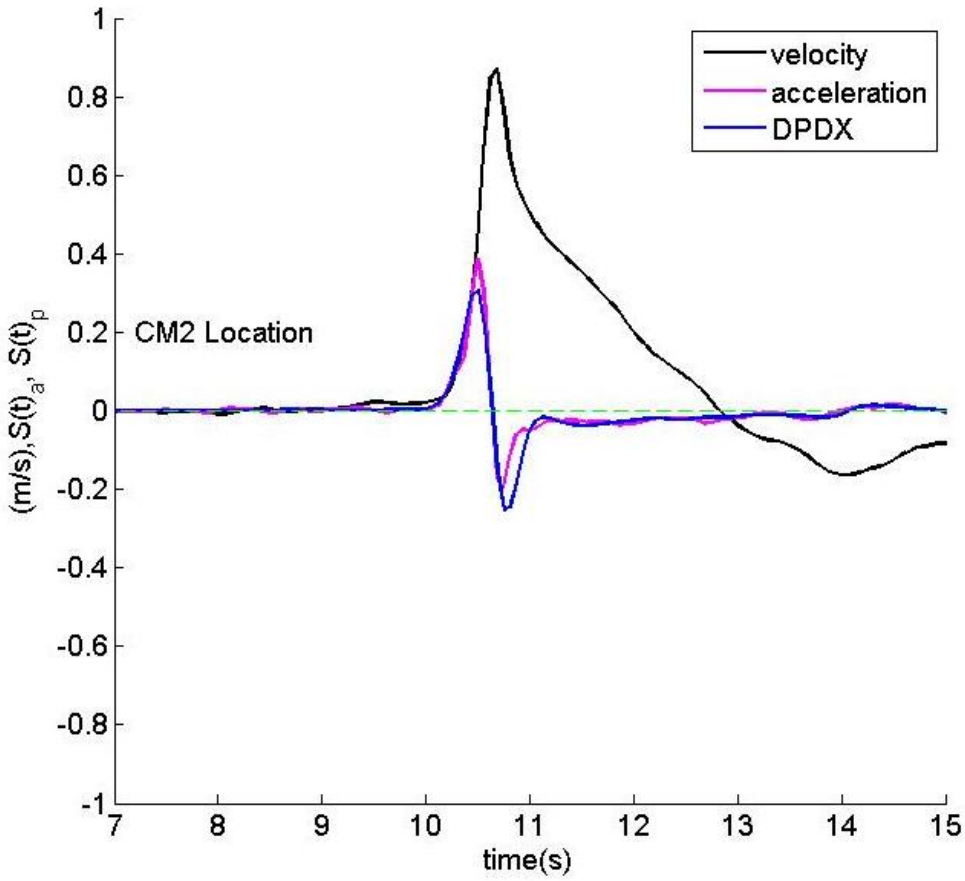

Figure 4.9: The velocity, acceleration, and horizontal pressure gradient for CM2 location are shown.

The sign of the velocity denotes whether the flow is moving onshore (+) or offshore (-) and the nearbed instantaneous acceleration is positive for fluid accelerating onshore and negative for flow accelerating in the offshore direction. While the flow is onshore-directed (+), a peak in the nearbed instantaneous acceleration has been shown to contribute to sediment suspension and onshore sediment transport. The Sleath

parameters for the nearbed accelerations and nearbed total pressure gradient at CM2 and over the 30 cm span of the nearshore sensor array are of similar magnitudes. $S(t)_a$ has a maximum value of 0.39 and $S(t)_p$ has a maximum value of 0.31. Both acceleration and pressure gradient have an onshore directed duration of 0.59s. This time span is equivalent to 20.63% of the duration of the onshore-directed velocity associated with the solitary wave at CM2.Also, the Sleath parameters are not only of the same magnitude, but are almost exactly in phase. This would suggest that horizontal gradients of total pressure are well-represented by the temporal fluid acceleration and thus could contribute to onshore sediment transport.

Chapter 5

NUMERICAL MODEL DESCRIPTION AND SETUP

5.1 COBRAS Description

In conjunction with the laboratory experiments, a numerical model study of the pressure gradients was also conducted. The model used in this study is the Cornell Breaking Wave and Structures (COBRAS) model. COBRAS is a phase- and depth-resolving wave propagation model. COBRAS uses a Volume of Fluid (VOF) method to determine the free surface of the fluid and the effects of turbulence are integrated by a coupling of the mean momentum equations and the transport equations of the turbulent kinetic energy and the dissipation rate. The governing equations for conservation of mass and momentum of the mean flow are, respectively.

$$\frac{\partial u_i}{\partial x_i} = 0 \quad , \qquad 14$$

$$\frac{\partial u_i}{\partial t} + u_j \frac{\partial u_i}{\partial x_j} = -\frac{1}{\rho}\frac{\partial p}{\partial x_i} + g_i + \frac{1}{\rho}\frac{\partial \tau_{ij}}{\partial x_j} \quad , \qquad 15$$

where i,j=1,2 for a two-dimensional flow. u_i is the i-th component of the velocity vector and τ_{ij} is the viscous stress tensor. To complete Equations (14) and (15), a k-ε closure scheme is use where k is the turbulent kinetic energy and ε is the turbulent dissipation rate:

$$\tau_{ij} = 2\left(\nu + C_d \frac{k^2}{\varepsilon}\right)\sigma_{ij} - \frac{2}{3}k\delta_{ij} \quad , \qquad 16$$

where C_d is a coefficient that relates k and ε to the eddy viscosity ν_t, δ_{ij} is the Kronecker delta, σ_{ij} is the rate of strain tensor, and ν is the kinematic viscosity (μ/ρ). The k-ε closure model is described in given as

$$\frac{\partial k}{\partial t} + u_j \frac{\partial k}{\partial x_j} = \frac{\partial}{\partial x_j}\left[\left(\frac{\nu_t}{\sigma_k} + \nu\right)\frac{\partial k}{\partial x_j}\right] + 2\nu_t \sigma_{ij} \frac{\partial u_i}{\partial x_j} - \varepsilon \quad \text{, and} \qquad 17$$

$$\frac{\partial \varepsilon}{\partial t} + u_j \frac{\partial \varepsilon}{\partial x_j} = \frac{\partial}{\partial x_j}\left[\left(\frac{\nu_t}{\sigma_\varepsilon} + \nu\right)\frac{\partial \varepsilon}{\partial x_j}\right] + C_{1\varepsilon}\frac{\varepsilon}{k} 2\nu_t \sigma_{ij} \frac{\partial u_i}{\partial x_j} - C_{2\varepsilon}\frac{\varepsilon^2}{k} \quad , \qquad 18$$

Where ν_t is the eddy viscosity, and $C_{1\varepsilon}$, $C_{2\varepsilon}$, σ_k, *and* σ_ε are empirical coefficients.

Since the total derivative of any physical property of free surface particles vanishes at the surface, the free surface can be tracked using density as the vanishing property.

$$\frac{\partial \rho}{\partial t} + u_i \frac{\partial \rho}{\partial x_i} = 0 \qquad 19$$

In the VOF method, the density of fluid in each computation cell is the average density of the entire cell. The free surface can be tracked by noting which cells in the domain have an average density that is less than that of the fluid but greater than the density of the air.

The COBRAS model provides a tool in the study of breaking waves for a variety of different wave structures and boundary conditions. One can examine the configuration of the free surface as well as determine the mean velocity, turbulent intensity, pressure, and pressure gradient fields for each simulation case.

5.2 Simulation Setup

To test the same experiment numerically, the specifications of the wave flume, the sensor locations, and wave forcing type are replicated within the bounds of the numerical model. The procedure to set up the numerical model is given in Figure 5.1.

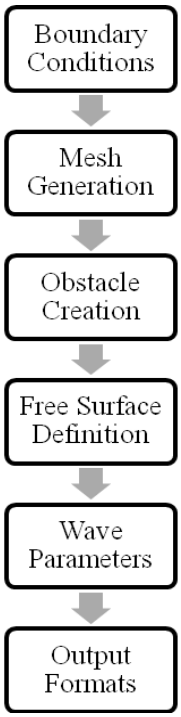

Figure 5.1: The COBRAS input file combines these elements to recreate the laboratory experiments

The input data (overviewed in Figure 5.1) are shown in detail in the appendix. This chapter will highlight only the parameters relevant to this test case.

5.2.1 Boundary Conditions

The boundary conditions can be defined in six different ways for the four boundaries of the computational domain (Figure 5.2).

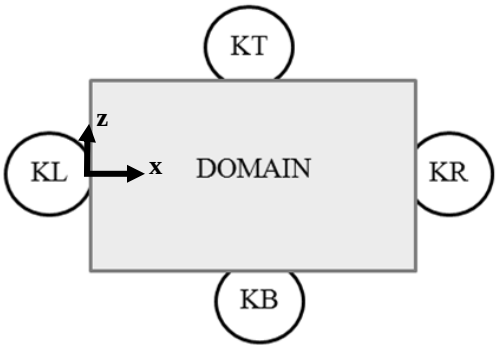

Figure 5.2: The computational domain of COBRAS is defined by the four boundaries: left (KL), right (KR), top (KT), and bottom (KB)

The six options for boundary conditions are rigid free-slip, rigid no-slip, open flow, periodic, applied pressure, and specified inflow/outflow. KL is an open flow boundary, KR is a rigid free-slip boundary, KT is a rigid free-slip boundary, and KB is a rigid no-slip boundary. Since the wave is created within the domain, it does not need to be defined at the left boundary as might be expected, and remains an open boundary to act as sponge layer for reasons discussed later.

5.2.2 Mesh Generation

The mesh, obstacles, and free surface can all be defined separately with several lines of code in the input file, or developed together with the use of a GUI, CORAL. 'Obstacles', in this instance, refers only to the geometry of the beach. The geometry of the numerical model wave flume varies from the experimental wave flume in two distinct ways. First, the distance from the left boundary of the wave flume to the beginning of the sloping beach is 10 meters greater in length than the Precision Wave Flume in the laboratory (Figure 5.3).

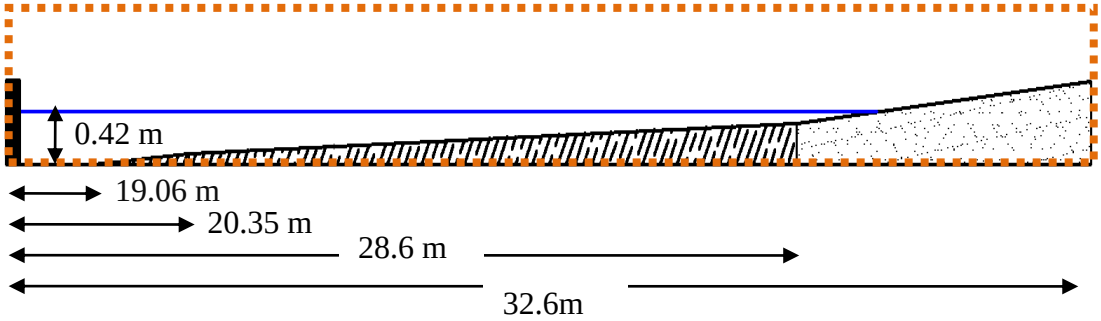

Figure 5.3: The wave flume is lengthened to do the model simulations.

The numerical model requires the additional length in the mesh in order to use the source function (see section 5.2.3) as the method of wave generation. The boxed area (Figure 5.3) is the computational mesh.

The second significant difference between the physical and numerical experiment is the use of a rotated reference frame for the numerical model (Figure 5.4).

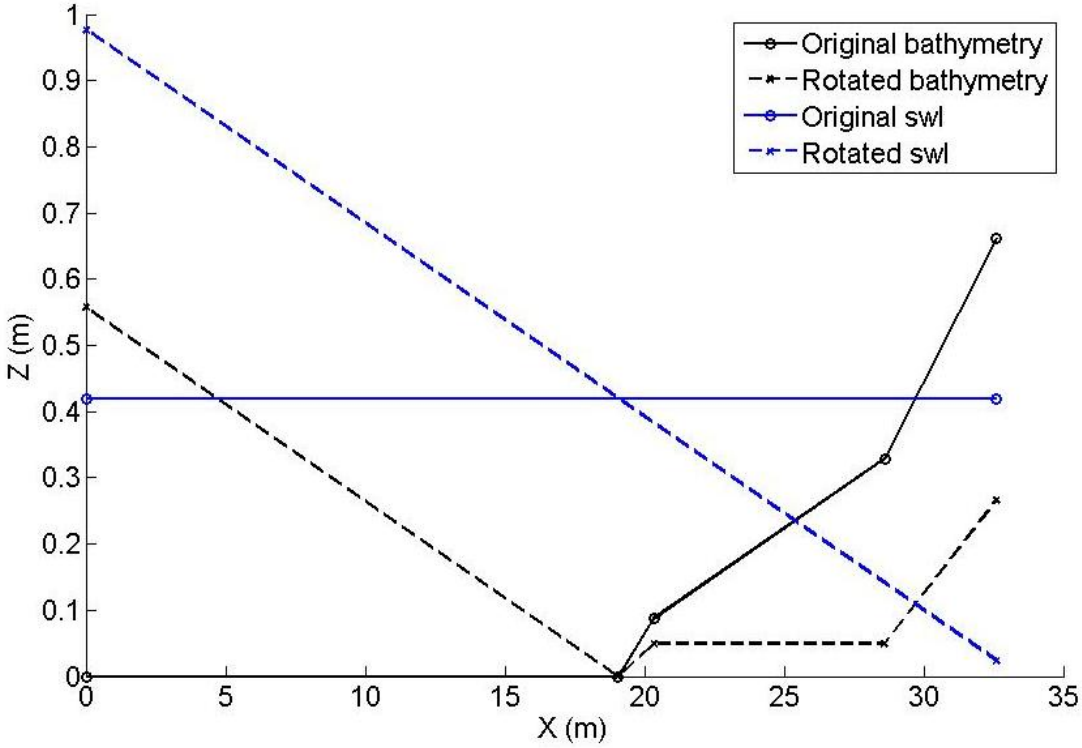

Figure 5.4: The experimental reference frame is rotated by 1.67º in the numerical reference frame.

In a real-world coordinate system, the surf and swash zones are sloping surfaces relative to the offshore sea-bed and the desired outputs from the numerical model are the near-bed measurements in the surf and swash zones. With a non-rotated frame of reference, the cells closest to the beach face will often have errors induced by the sloped obstacle, since the slope is composed of a series of very small horizontal steps. It then becomes expedient to have the location where the majority of the data will be extracted to be over a horizontal boundary. To do this, the bathymetry is rotated and

the 1:34.2 slope becomes parallel with the X-axis (Figure 5.4). The X- and Z-components of gravity are altered accordingly.

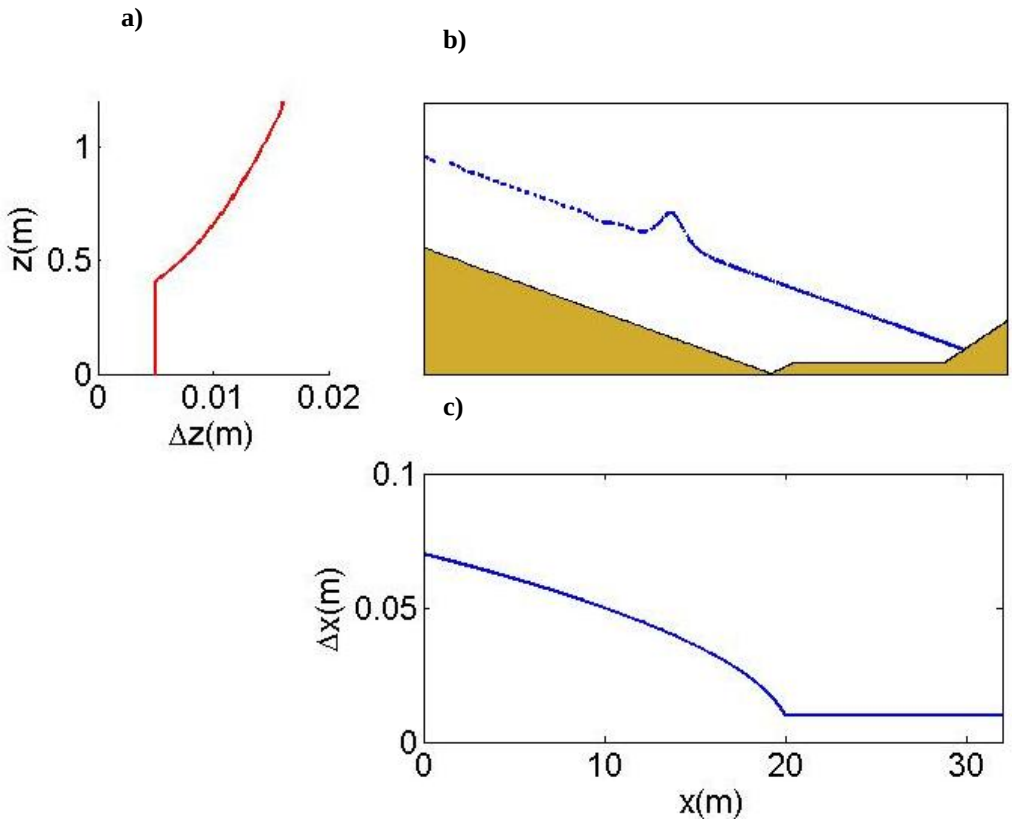

Figure 5.5: The rotated reference frame has variable grid spacing in both the X- and Z-direction.

The mesh needs to be small enough to have a good resolution in the inner surf and outer swash zone, but large enough so that computation is still feasible. The solution is a mesh grid that is variable in both the X- and Z- direction (Figure 5.5). The rotated computation region (Figure 5.5b) is 1.2 m in the Z-direction, the mesh reduces from a 0.016 m at the KT boundary to 0.005 mat z= 0.4 m (Figure 5.5a). From z=0.4 to z=0, the KB boundary, the grid spacing is a constant0.005 m. In the X-direction the grid

spacing varies from 0.065 m offshore at KL and reduces to 0.01 m at x=20.00 m, and then the grid spacing remains constant throughout the surf and swash zones (Figure 5.5c). The mesh in both directions reduces where the calculations are more important and a higher resolution is needed.

5.2.3 Wave Generation

The solitary wave is defined using a source function. Generating waves from a boundary and having the capacity to absorb reflected waves at the same boundary can be a challenge. One way to manage this difficulty is by using an internal wave maker in the form of a source function. The source function method uses mass source functions for the equation of mass conservation within the computational mesh instead of applying a wave inducing condition at the left inflow boundary. The source function is design so as not to interact with reflected waves. This method works to generate linear monochromatic waves, irregular waves, Stokes waves, cnoidal waves, and solitary waves. The veracity of these models is well-documented and the results of a comparison between numerical and analytical wave heights are almost identical with decreasing accuracy as the ratio of wave height to water depth increases. The reduction in accuracy is partially due to the fact that solitary wave theory itself fails at higher wave height to water depth ratios (Lin and Liu, 1999).

The source function generates a system of waves that propagates in two directions (positive and negative X-axis). The wave that propagates offshore is absorbed by an added sponge layer. In this test, the left boundary was left open, because in previous tests, an open KL boundary performed better in the numerical model when testing solitary wave conditions. To use the source function in COBRAS, the flume dimensions were manipulated in the X-direction. There are approximately

two wavelengths between the KL boundary and the source location and between the source location and the offshore wave gauge. Solitary waves are of infinite wave length by definition. However, solitary waves have an effective length that can be described by a simple equation:

$$l = \frac{2.12h}{\sqrt{a/h}}, \qquad 20$$

Where h is the water depth, a is the wave amplitude and l is the effective length of the solitary wave that contains 95% of the wave volume (Dean and Dalrymple, 1991). The added space between the left boundary and between the first wave gauge allows for proper generation of the target wave and improves results. The source function generated wave has the same target wave height (15.00 cm) as in the laboratory experiment.

Chapter 6

NUMERICAL MODEL RESULTS

The solitary wave test simulation was completed using the source function as a forcing mechanism and calculated over a 1742x157 mesh. The resulting output yields a 25 second record of the wave breaking, running up the beach and propagating back offshore.

The numerical model can offer much greater detail than the series of sensors used in the laboratory experiment. This, however, only provides useful information if the numerical model is true to the physical processes occurring in the wave flume.

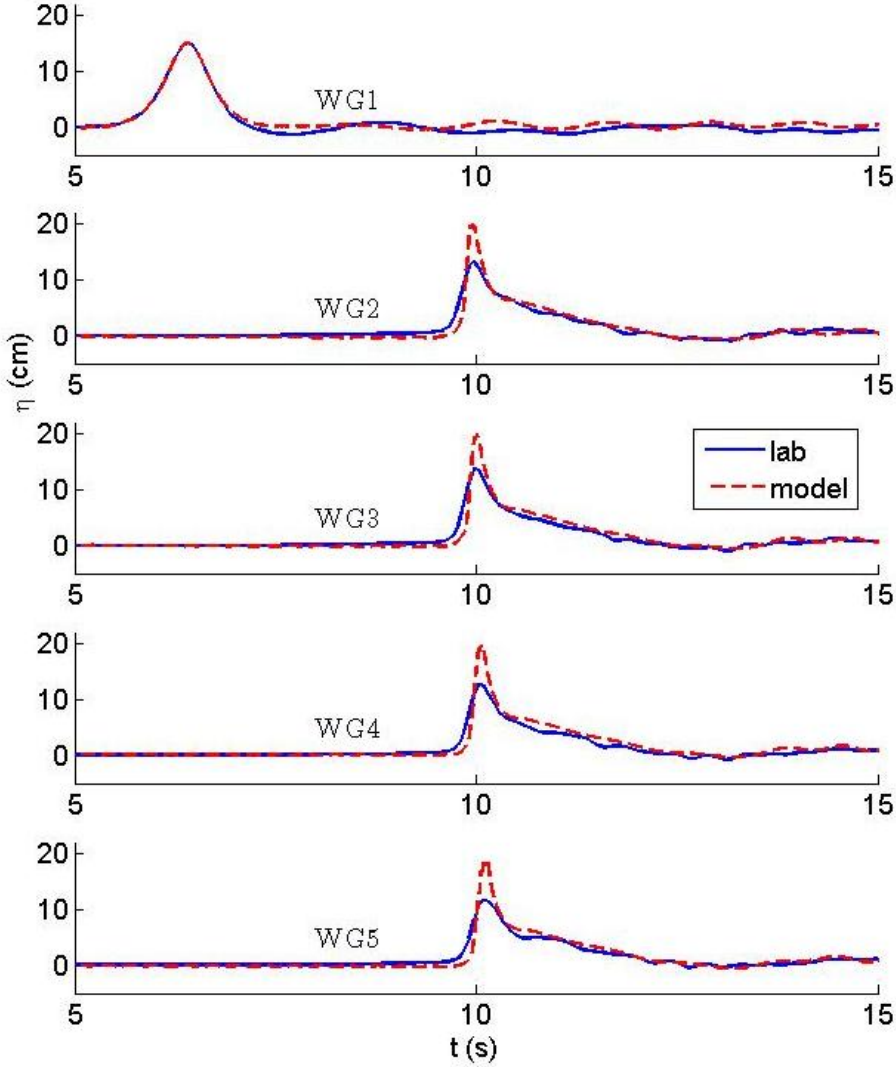

Figure 6.1: The free surface is shown at each of the wave gauge locations for both the numerical model and the laboratory experiment.

The first comparison between the numerical model data and the experimental data is that of the free surface (Figure 6.1). In the numerical model a wave gauge was inserted at the same cross-shore location as seen in the Precision

Wave Flume. Figure 6.1 shows these co-located wave gauges from each source. The numerical model replicates the offshore solitary wave almost perfectly at the WG1 location. At WG2-5, the wave gauges onshore of the breakpoint, the model-experiment agreement is not nearly as good.

Table 6.1: Peak Hp for experimental and model solitary waves

	Exp. H_p (cm)	Model H_p (cm)
WG1	14.98	15.08
WG2	13.38	19.95
WG3	13.69	20.06
WG4	12.73	19.83
WG5	11.77	19.09

The main issue with the data agreement is that the peak values for each peak wave height, H_p, do not match (Table 6.1). The difference can be as much as 38.33% at WG5. One possible reason for this large discrepancy is the ability of the model to predict wave breaking. In the Precision Wave Flume, the wave breaks at x=16.1m. In COBRAS, the wave breaks at x=16.95m.

Lin and Liu (1998) state that due to limitations of the numerical model and uncertainty in the initial and inflow boundary conditions for the turbulent kinetic energy causes difficulties in prediction of the breaking point. The model has trouble fully capturing the intricacies of the overturning jet of water at breaking. The model recovers its accuracy onshore of the breaking location.

One method of dealing with this discrepancy is by comparing the mean flow fields of the experimental and model wave at the same cross-shore location after breaking, x_b.

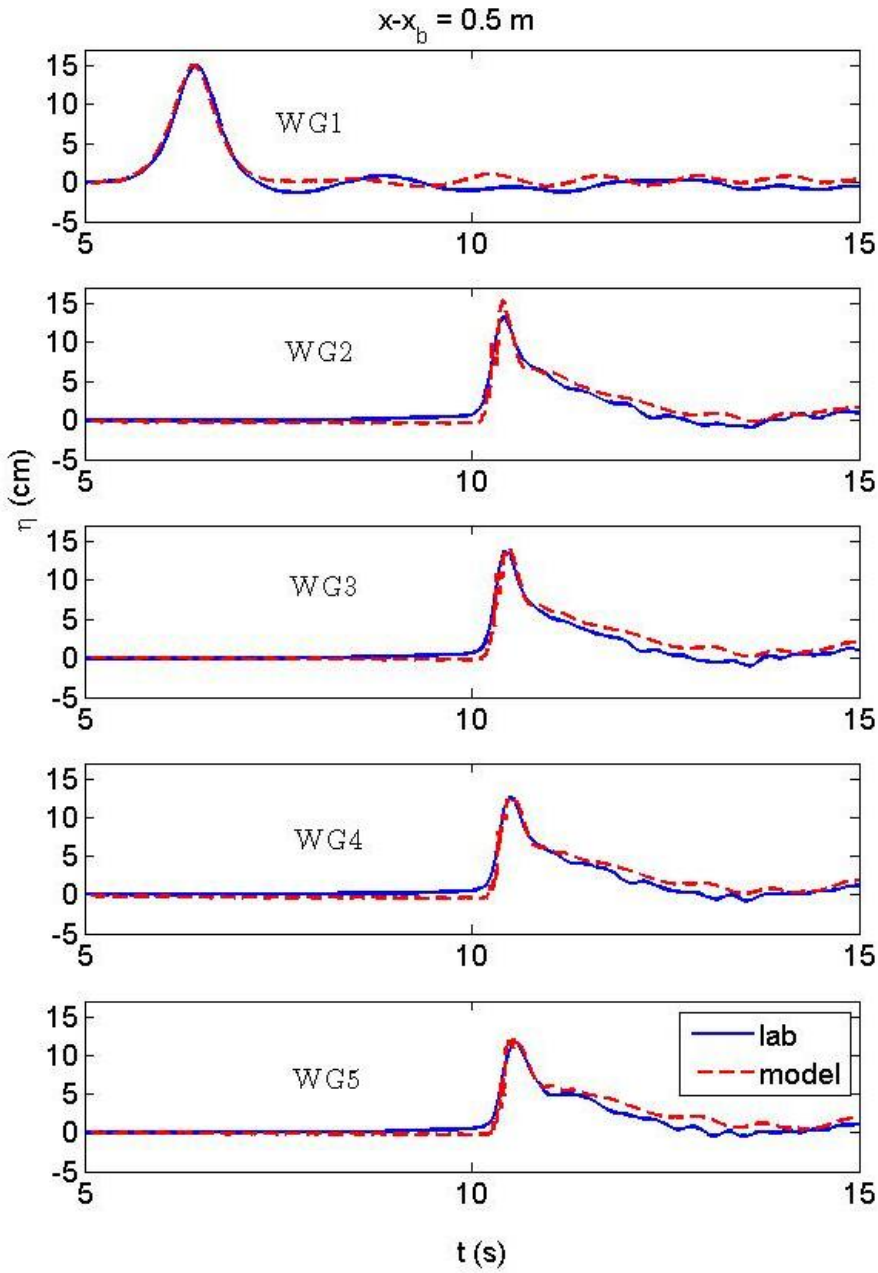

Figure 6.2: The free surface of the solitary wave from the lab and numerical model data at $x-x_b$=0.5 m

Table 6.2: Peak Hp for experimental and model solitary waves at $x-x_b$=0.5 m

	Exp. H_p (cm)	Model H_p (cm)
WG1	14.98	15.08
WG2	13.38	15.38
WG3	13.69	13.89
WG4	12.73	12.8
WG5	11.77	12.13

Figure 6.2 and Table 6.2 offer a comparison between the experimental data and the numeral wave gauge data at $x-x_b$=0.5 m. When the data are viewed at the same post-breaking location, the peak wave heights have much better agreement with a maximum difference of 13% at WG2, a significant improvement upon Table 6.1.

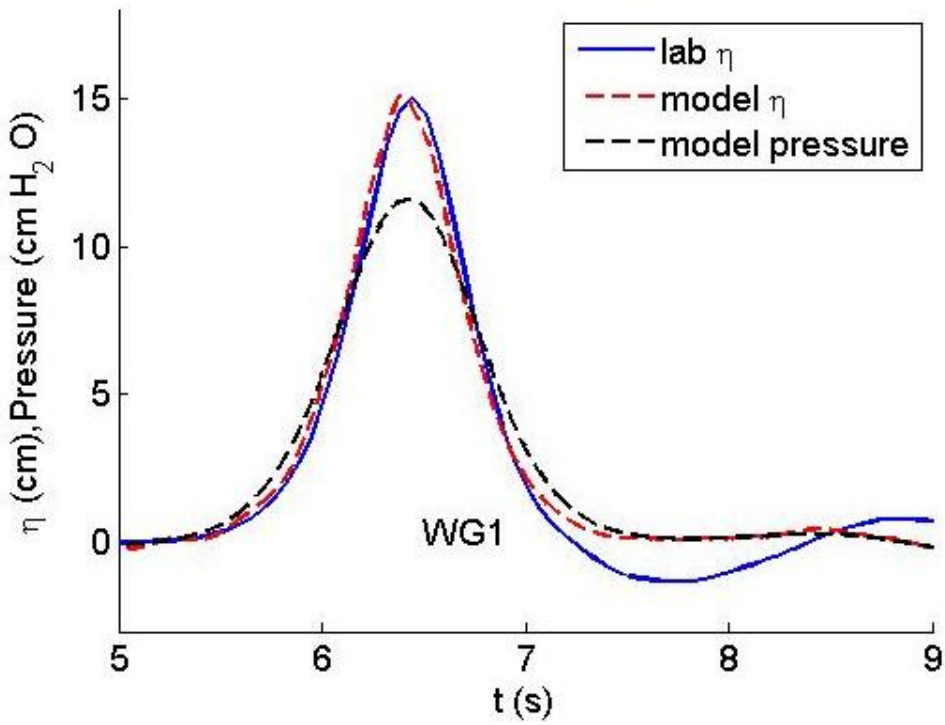

Figure 6.3: The offshore model and experimental free surface are overlaid with a time series of the model total nearbed pressure.

At the offshore measurement location, the x-x_b shift of the data measurement does not affect the comparison between the lab and model data. What is interesting to note at this location is that the peak in the total pressure, in terms of cm of H_20, is lower than the peak of the free surface. While this finding may seem counterintuitive, it is the expected theoretical pressure for an unbroken solitary wave (Svendsen, 2006).

The pressure under the wave after breaking (Figure 6.4) extracted from the model shows how the turbulent flow introduces large fluctuations in the nearbed pressure.

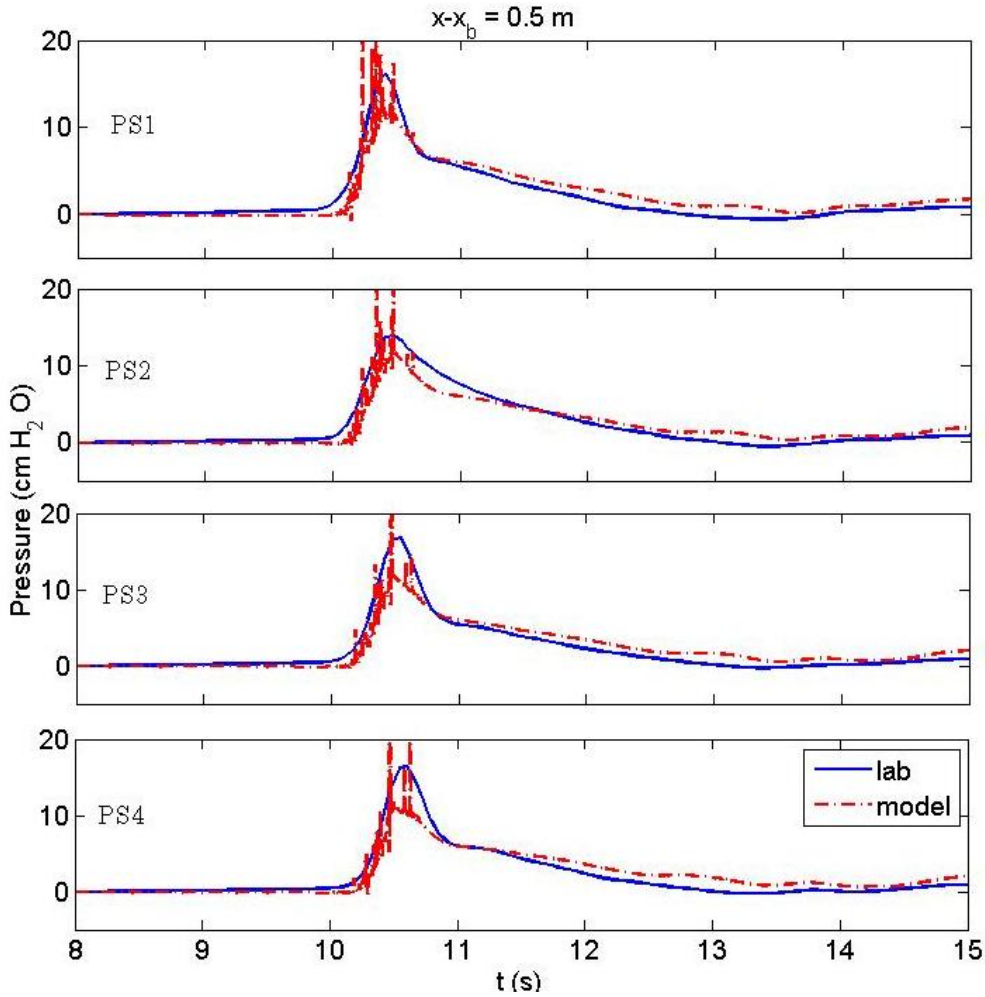

Figure 6.4: The nearbed pressure under the solitary wave from the lab and numerical model data at $x-x_b$=0.5 m

The agreement of the model/data for the pressure sensors is highlighted in Figure 6.4 and Table 6.3.

Table 6.3: R^2 values comparing the pressure of the numerical model with the experimental data

	R^2 Value
PS1	0.96
PS2	0.98
PS3	0.96
PS4	0.96

At each nearbed pressure sensor location, the total pressure extracted from the numerical model accurately predicts the shape and the general magnitude of the pressure in the laboratory experiment for the initial onshore-directed wave motion.

Figures 6.3 and 6.4 would indicate that the model predicts the general trends of the pressure over the entire domain, based on the compared locations. The differences at the locations after the breakpoint would most likely be attributed to the model's difficulty resolving hydrodynamic conditions during and shortly after breaking. To isolate the dynamic pressure and the dynamic pressure gradient, the hydrostatic pressure, or the pressure related to the free surface needs to be subtracted from the total pressure. Due to turbulence in the model total pressure output, subtracting the hydrostatic pressure from the total pressure will not yield useful representation of the dynamic pressure. Yet, since the magnitude of the pressure gradients are similar between model and experiment and both have peak values larger than the hydrostatic values, the development and change of the total pressure gradient during the solitary wave event can be further studied.

The velocity and pressure gradient time series (Figures 6.5 and 6.6) show the level of agreement between the model and experimental data for those two flow parameters.

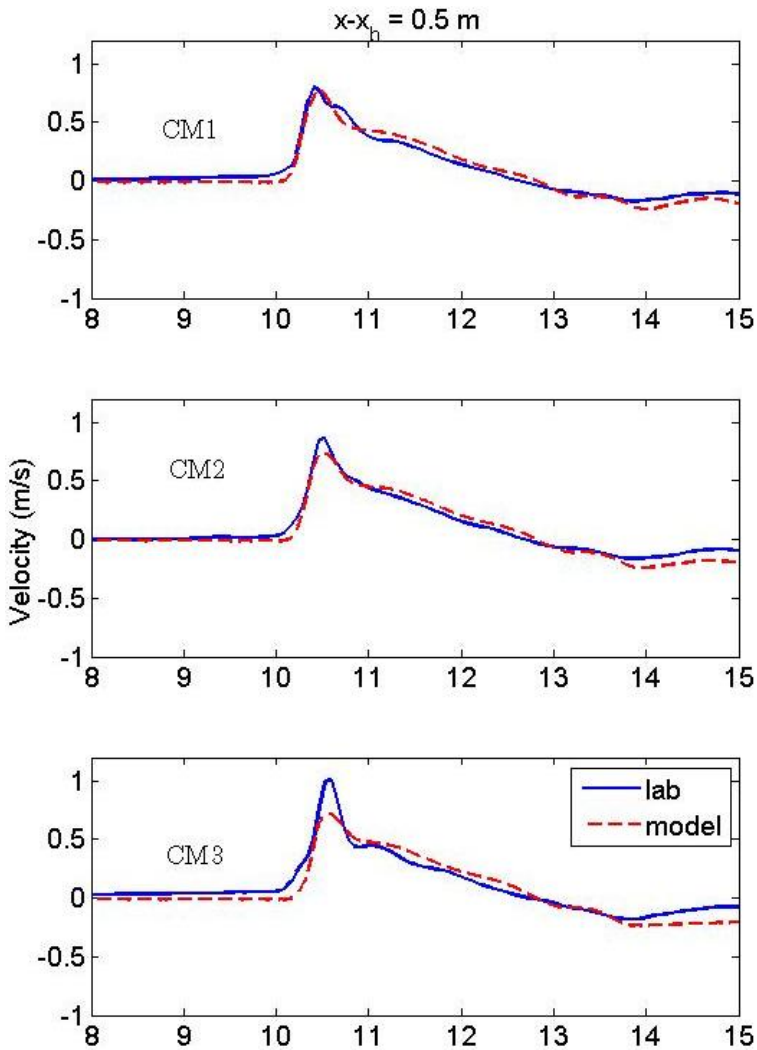

Figure 6.5: The cross-shore velocity is shown at EMCM location for both the numerical model and the laboratory experiment.

Table 6.4: R^2 values comparing the velocity of numerical model with the experimental data

	R^2 Value
CM1	0.98
CM2	0.98
CM3	0.96

The numerical model is capable of (Table 6.4) predicting the velocity for CM1, CM2 and CM3.

All of the numerical fluctuations present in the model's pressure output translate to the model's pressure gradient output. The non-dimensional total pressure gradient of the numerical model shown with the experimental total pressure gradient (Figure 6.6) has correlation ranging from 0.96 to 0.98 at the Nearshore Sensor Array in spite of the fact that the measurements occur directly after breaking.

The expected trend of the pressure gradient is shown in each DPDX location in comparing the pressure gradient (Figure 6.6). To further look at the pressure gradient, the Δx value is varied from 10 cm to 30 cm, which is the maximum spacing of the experimental pressure sensors in the Nearshore Sensor Array.

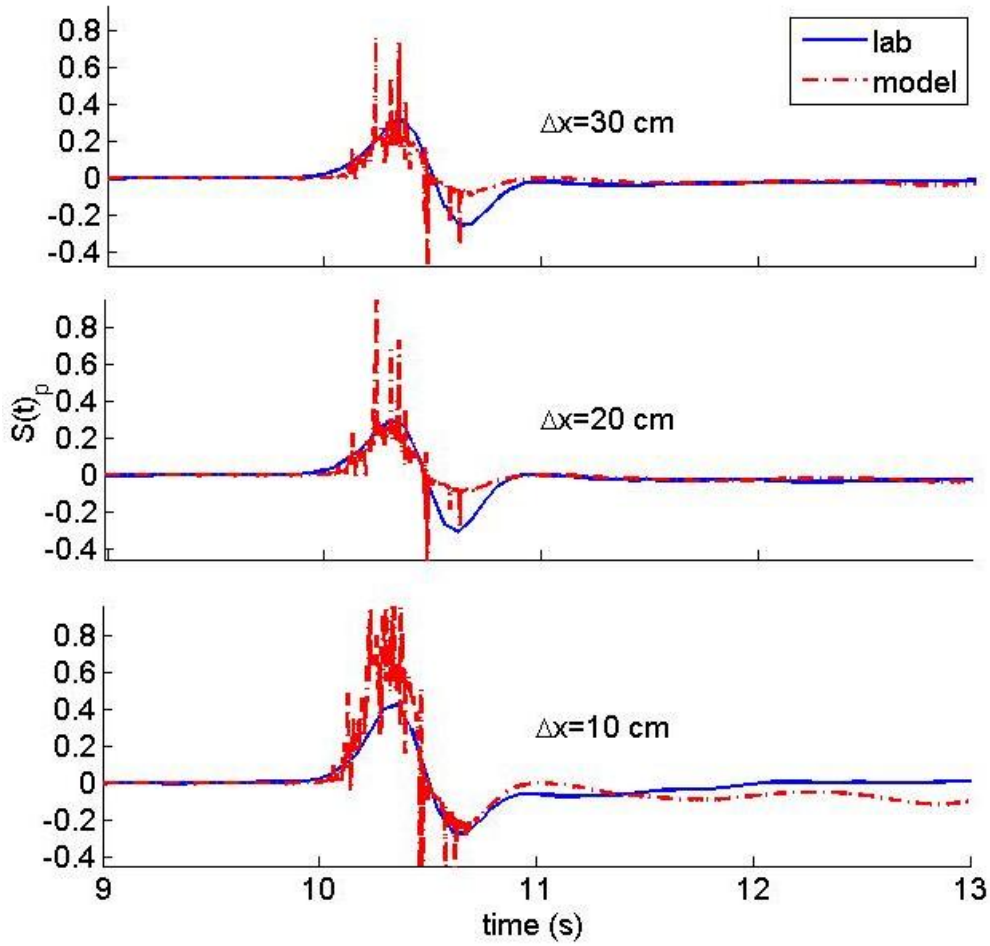

Figure 6.6: The total horizontal pressure gradient calculated three different pressure sensor spacings.

The numerical horizontal pressure gradient calculated from PS1 and PS4 has a good agreement with the experimental horizontal pressure gradient (Table 6.5).

Table 6.5: R^2 values comparing the pressure gradient of numerical model with the experimental data

	R^2 Value
Δx=10	0.92
Δx=20	0.91
Δx=30	0.92

The positive magnitudes of each are similar, as are the phase and duration. The adverse pressure gradients show a large difference in magnitude. The numerical model prediction has the pressure gradient skewed to be onshore-directed, while the experimental pressure gradient shows a more symmetric pressure gradient.

The pressure gradient, among other parameters, can be shown for the entire computational regime (Figure 6.7).

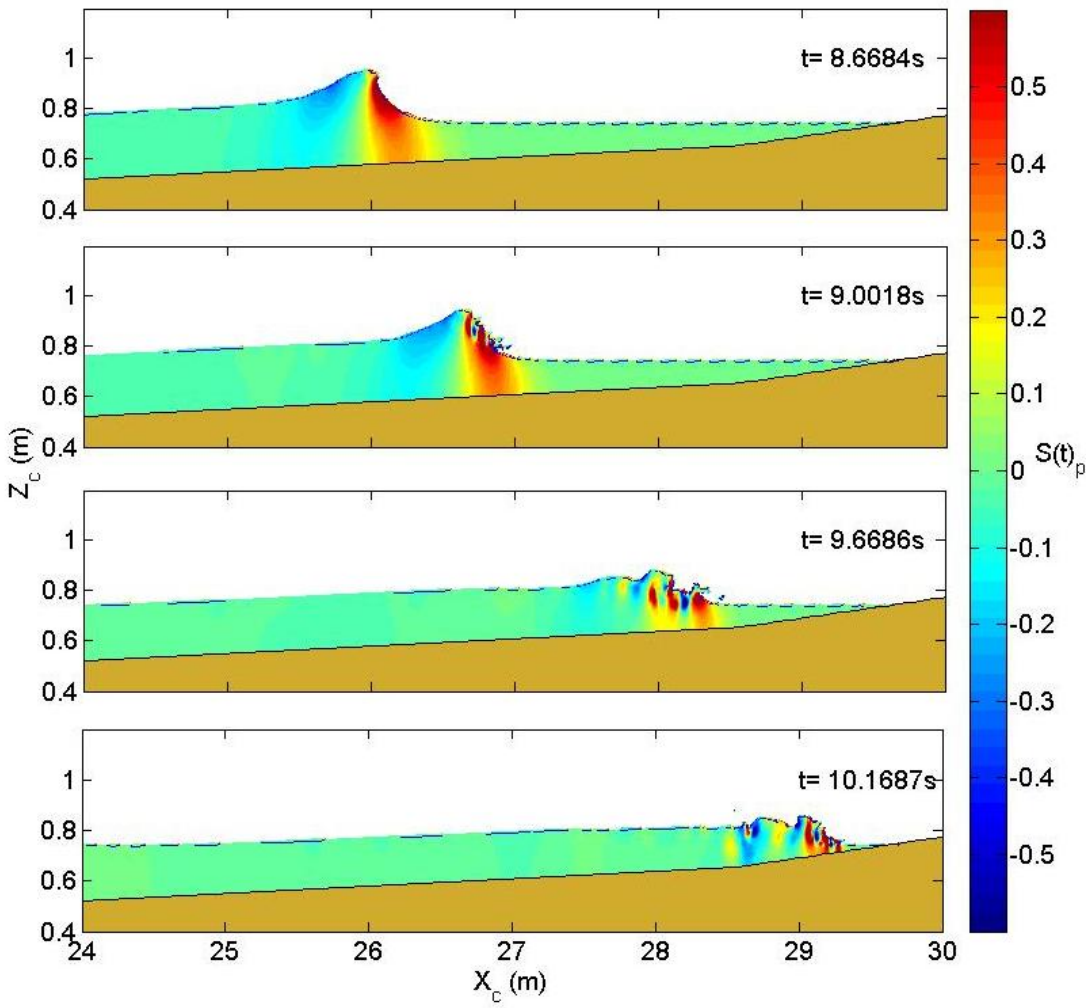

Figure 6.7: The solitary wave propagates onshore in this series of numerical model snapshots, where the color scale is the total pressure gradient.

The solitary wave breaks after 8.7 seconds in the simulation (Figure 6.7). While the wave moves shoreward, there is a strong onshore force due to the pressure gradient throughout the entire water column under the leading edge of the wave. There is also,

of course, an adverse pressure gradient under the trailing edge of the wave, but its magnitude is smaller, and it rarely penetrates to the bottom of the water column.

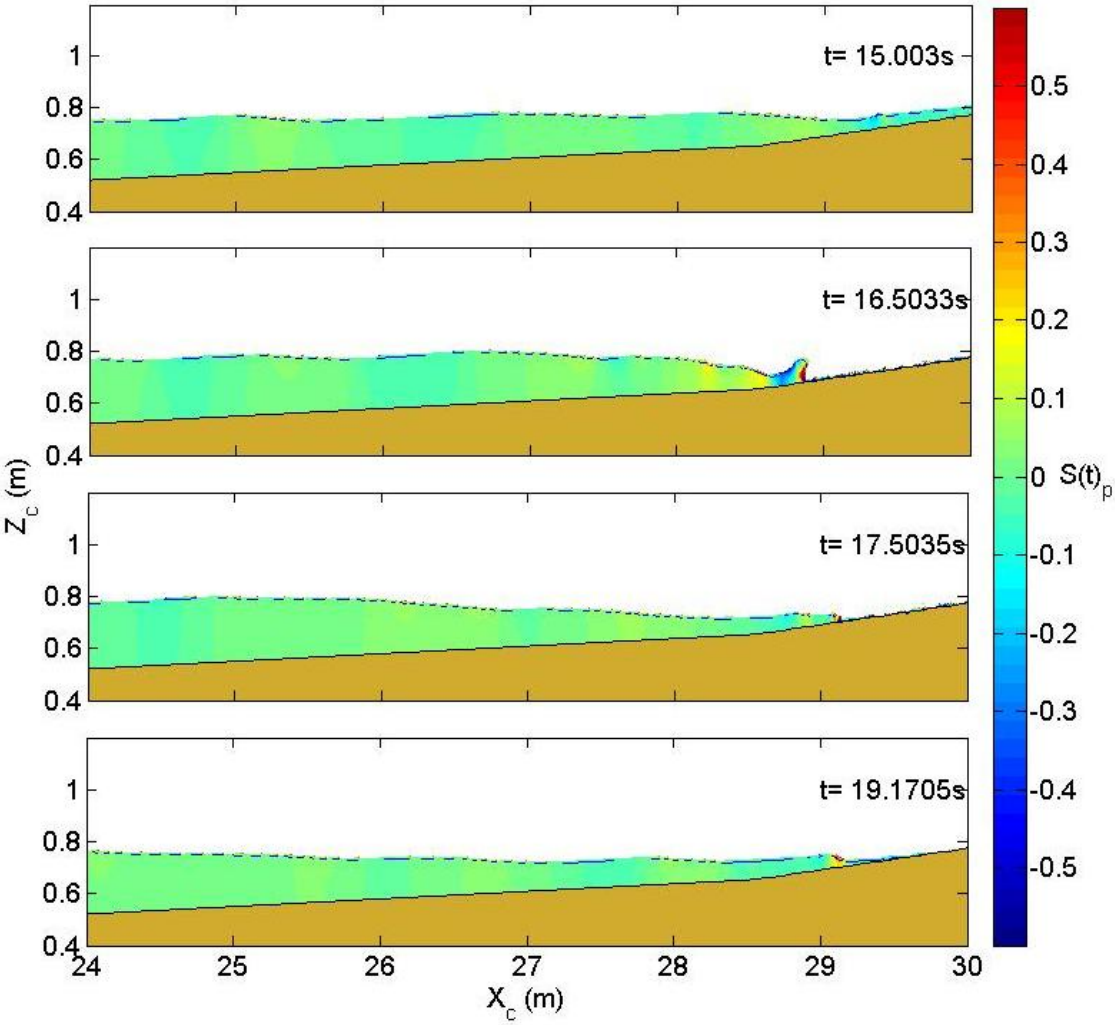

Figure 6.8: The solitary wave propagates offshore in this series of numerical model snapshots, where the color scale is the total pressure gradient.

After flow reversal (Figure 6.8), the pressure gradient is quite small and is only nonzero for a short duration. In order to enhance sediment transport, the pressure

gradient needs to reach the sediment at the bed. Figure 6.10 presents a closer look at the nearbed pressure gradient, as well as the horizontal velocity for an entire wave cycle using a time-stacking procedure.

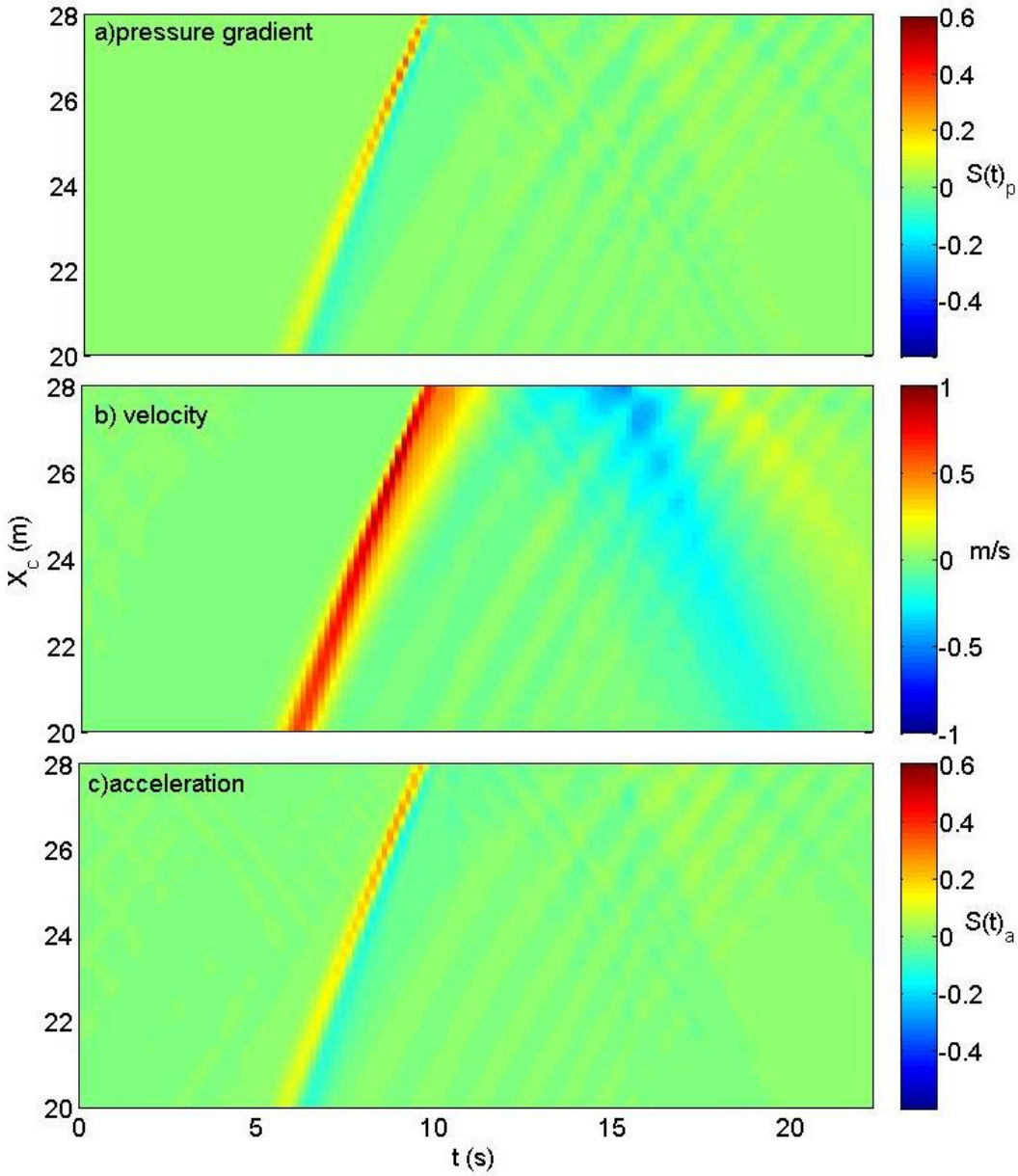

Figure 6.9: A time stack represents a)the nearbed horizontal pressure gradient b) the nearbed horizontal velocity and c) the acceleration taken from the first grid point above the bed and twelve grid points from the bottom of the computational mesh

Figure 6.9a-c shows a time stack of the total pressure gradient, the near-bed horizontal velocity, and the acceleration (color scale). Although snapshots (Figure 6.7, Figure 6.8) are useful in providing spatial information about the wave motion, they are by nature restricted to a particular time. Time stacks overcome this temporal limitation by stripping the pressure gradient values from any bed orthogonal level to show the progression of the swash motion in a space-time plot. Since the pressure sensors for the laboratory experiment will be nearly bed-level, the second grid point above the bed was the elevation for data extraction. In this figure "nearbed" refers to the 1:34.2 slope and not the steeper 1/12 slope. This is the reason why the data are "cut-off" at X_c=28m. Beyond that point, there is the solid boundary of the steeper beach face.

The total pressure gradient is largest during the strong onshore velocities. The model run shows that the pressure gradient is negligible throughout the rest of the wave cycle. Even when the flow accelerates offshore shortly after flow reversal, the pressure gradient close to the bed is zero. The acceleration and pressure gradient are very similar, but the peak values of the non-dimensional pressure gradient are higher than the peak values of acceleration (Figure 6.10).

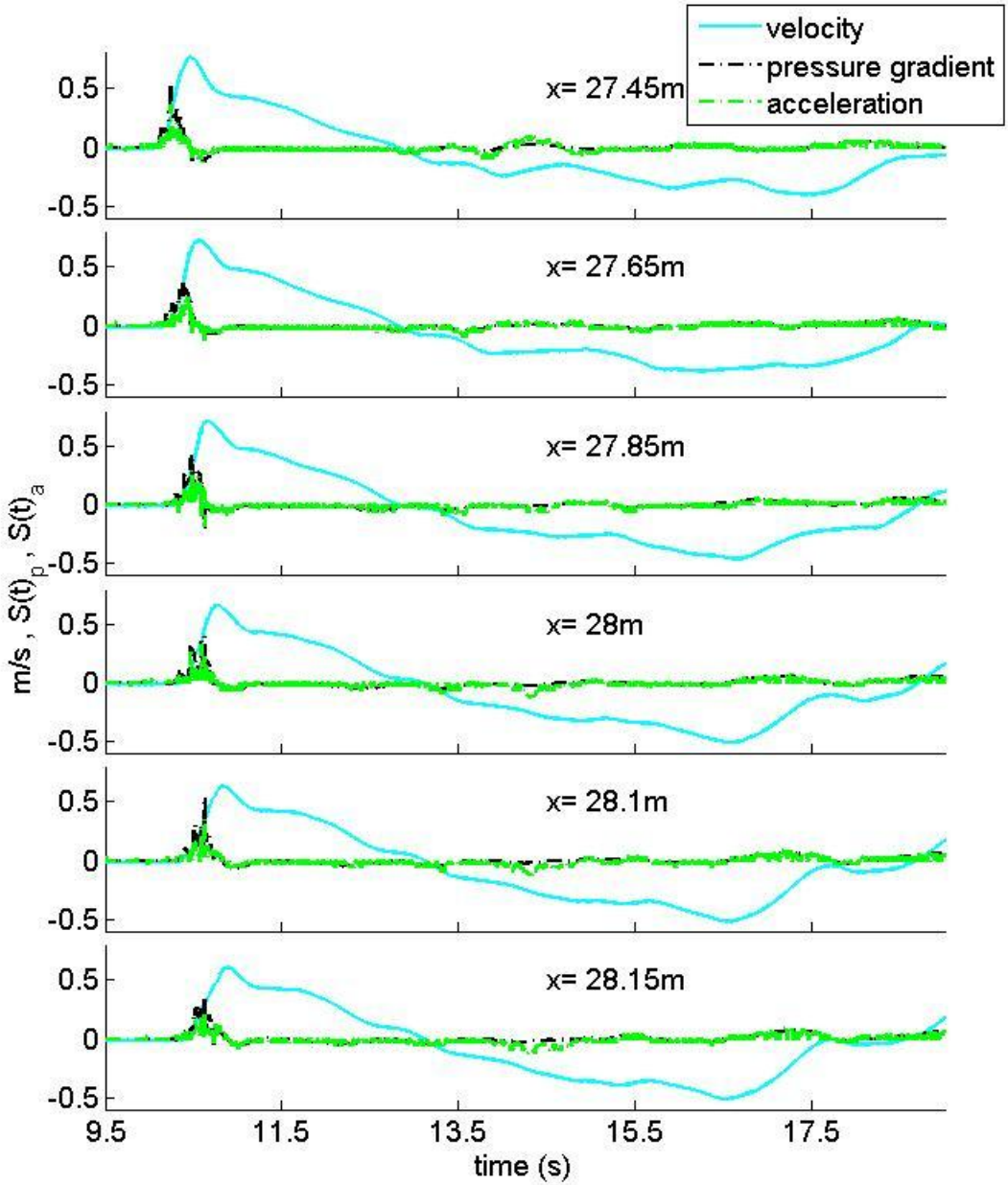

Figure 6.10: Model extracted time series of the nearbed velocity, pressure gradient, and acceleration

At each pressure sensor and wave gauge location in the model in the inner surf zone, the peak value is larger than the acceleration, and they are in phase. The model extracted time series allow a look at these values farther onshore than would be possible in the laboratory, due to the physical restrictions of the experimental pressure sensors. Using the acceleration as an approximation would yield a similar result to the pressure gradient, but during the moments when the pressure gradient is most important, the acceleration would underestimate the magnitude by a maximum of 34.5% at the peak.

Chapter 7

CONCLUDING REMARKS

A total of 10 solitary wave tests were conducted in a laboratory wave flume to investigate the horizontal pressure gradient under a wave. A new pressure measurement technique was used to collect information about the total pressure close to the bed in regions of the beach that remained fully submerged. The tests were ensemble averaged for the results. The experimental tests showed that using the nearbed pressure sensors instead of a proxy yielded a higher shoreward pressure gradient in the surf zone under a passing wave.

During each experimental test, eight pressure sensors were deployed in the inner surf zone in pairs. Five wave gauges were also used. One wave gauge recorded the offshore wave height and the other four were placed at the same cross-shore location as each pressure sensor pair. Between each pressure sensor location, an electromagnetic current meter recorded the velocity for a total of three current meters. The ensemble averaged velocity was used to evaluate the acceleration. The ensemble averaged pressure time series were used to calculate the horizontal pressure gradient and the four onshore wave gauges are used to determine the hydrostatic pressure under the solitary wave.

The experimental procedure was repeated using a numerical model, COBRAS. The model matched all of the experimental parameters in the unbroken solitary wave. After breaking, the model still showed relatively good agreement for the pressure, pressure gradient, velocity and free surface, in spite of the model's

difficulty with predictions during and directly after breaking. The pressure gradient of the model was similar in shape and magnitude to the experimental results. Since the experimental pressure sensors must remain fully submerged to work properly, the numerical model provides useful insight into the pressure gradient farther onshore than what can be measured in the lab. The nearbed pressure gradient is favorable for most of the shoreward portion of the wave cycle and negligible during the offshore flow. The implications are that the horizontal pressure gradient could be a contributing factor to beach accretion. To further investigate this claim; more experimental and numerical studies should be done, at a minimum for a series of monochromatic waves and irregular waves.

BIBLIOGRAPHY

Bailard, J. A. (1981), An energetics total load sediment transport model for a plane sloping beach, J. Geophys. Res., 86, 938–954.Bagnold, R., A., 1956. The flow of cohesionless grains in fluids. Phil. Trans. Roy. Soc. Lon: 964(249), 235-297.

Bagnold, R.A., 1963. Beach and nearshore processes: Part 1. Mechanics of Marine Sedimentation. The Sea: Ideas and Observations, vol. 3. Interscience, New York, pp. 507– 528.

Bagnold, R.A., 1966. An approach to the sediment transport problem from general physics. U.S. Geol. Surv. 422-I, 11 – 137.

Baldock, T.E., Barnes, M.P., Hughes, M.G., 2006. Field observations of instantaneous crossshore free surface profiles and flow depths in the swash zone. In: Sanchez-Archilla, A. (Ed.), Coastal Dynamics 2005 [CD-ROM]. ASCE, Reston, VA.

Battjes, J. A. 1988 Surf-zone dynamics. *Ann. Rev. Fluid. Mech.* 20**,** 257-293.

Bowen, 1980. A.J. Bowen, Simple models of nearshore sedimentation; beach profiles and longshore bars. In: *The Coastline of Canada*S.B. McCann, Editor, *Geological Survey of Canada, Paper 80-10* (1980), pp. 1–11.

Butt and P.E. Russell, Suspended sediment transport mechanisms in high-energy swash, *Mar. Geol.* 161 (1999), pp. 361–375.

Butt, T., Russell, P., 2000. Hydrodynamics and cross-shore sediment transport in the swash zone of natural beaches: a review. J. Coast. Res. 16, 255±268.

Butt, T., Russell, P.E., Miles, J., Turner, I.L., 2007. Sediment transport processes in the swash zone of sandy beaches. International Coastal Symposium. Journal of Coastal Research 50, 636–640 (Special Issue).

Calantoni, J., Puleo, J.A., 2006. Role of pressure gradients insheet flow of coarse sediments under sawtooth waves. Journal of Geophysical Research 111, C01010.

Calantoni, J., Holland, K.T., Drake, T.G., 2004. Modelling sheet-flow sediment transport in wave-bottom boundary layers using discrete-element modelling. Philosophical Transactions of the Royal Society of London Series A—Mathematical Physical and Engineering Sciences 362 (1822), 1987–2001.

Crossett, Kristen M., et al., *Population Trends Along the Coastal United States:1980-2008*. National Oceanic and Atmospheric Administration National Ocean Service. September 2004.

Dean, Robert G., and Robert A. Dalrymple, *Water Wave Mechanics for Engineers and Scientists.*World Scientific Publishing Co. Pte. Ltd, 1991.

Drake, T. G., and J. Calantoni (2001), Discrete particle model for sheet flow sediment transport in the nearshore, J. Geophys. Res., 106, 19,859–19,868.

Elfrink, B., and T. E. Baldock (2002), Hydrodynamics and sediment transport in the swash zone: a review and perspectives, Coastal Eng., 45, 149–167.

Foster, D. L. Dynamics in the nearshore wave bottom boundary layer, Ph.D. thesis, 114 pp., Oregon State Univ., Corvallis,1996.

Foster, D.L., Bowen, A.J., Holman, R.A., and Natoo, P. _2006_. "Field evidence of pressure gradient induced incipient motion." *J. Geophys. Res.*, 111, C05004.

Allen, J. S., Henderson, S. M., and P. A. Newberger (2004), Nearshore sandbar migration predicted by an eddy-diffusive boundary layer model, J. Geophys. Res., 109, C06024.

Hibberd, S., and D. H. Peregrine, Surf and run-up: a uniform bore, J. Fluid. Mech., 95, 323-345, 1979.

Hicks, B., N. Kobayashi, J. Figlus, Cross-Shore Transport on Gravel Beaches. Center for Applied Coastal Research, Research Report No CACR-10-01 July 2010.

Holland, K. T., and J. A. Puleo, Variable swash motions associated with foreshore profile change, J. Geophys. Res., 106(C3), 4613– 4623, 2001.

Holman, R. A., and A. H. Sallenger Jr., High-energy nearshore processes, Trans. AGU, 67, 1365-1369, 1986.

Horn, D.P. and Mason, T., 1994. Swash zone sediment transport modes. Marine Geology, 120, 309-325.

Hughes, M. G., and T. E. Baldock (2004), Eulerian flow velocities in the swash zone: Field data and model predictions, J. Geophys. Res., 109, C08009, doi:10.1029/2003JC002213.

Hughes, M.,G., G. Masselink, and R. W. Brander, Flow velocity and sediment transport in the swash zone of a steep beach, Mar. Geol., 138, 91-103, 1997.

Iribarren, C.R., Nogales, C., 1949. Protection des ports. Sect. 2, comm. 4, 17th Int. Nav. Cong., Lisbon, p. 31– 80.

Kirkgoz, M.S., 1981, a theoretical study of plunging breakers and their runup: Coastal Engineering, v. 5, p. 353–370.

Kobayashi, N., G. S. DeSilva, and K. D. Watson, Wave transformation and swash oscillation on gentle and steep slopes, J. Geophys. Res., 9J, 951-966, 1989.

Kobayashi, N.; Orzech, M.; Johnson, B., and Herrman, M., 1997. Probability modelling of surf zone and swash dynamics. Proc. Waves '97 (ASCE), pp. 107-121.

Lin, P., and P. Liu, (1999), Internal Wave-Maker for Navier-Stokes Equations Models, J. of Waterway, Port, and Ocean Engineering, Vol. 125, No. 4, 207-215,July/August.

Lin, P., and W. Xu (2005), NEWFLUME: A numerical water flume for two dimensional turbulent free surface flows, J. Hydraul. Res., 44, 79–93.

Madsen, O. S. (1974), Stability of a sand bed under breaking waves, in Proceedings of 14th Conference on Coastal Engineering, pp. 776– 794, New York.

Masselink, G. and J. A. Puleo (2006), Swash-Zone Morphodynamics, Cont. Shelf Res. 26 (2006) 661–680

Masselink, G. and M. Hughes, Field investigation of sediment transport in the swash zone, Cont. Shelf Res. 18, 1179-1199, 1998.

Masselink, G., and L. Li (2001), The role of swash infiltration in determining the beachface gradient: A numerical study, Mar. Geol., 176, 139–156.

Puleo, J. A. (2004), Hydrodynamics and sediment transport in the inner surf and swash zones, Ph.D. thesis, 280 pp., Univ. of Fla., Gainesville.

Puleo, J. A., and T. Butt (2006), The 1st international workshop on swashzone processes, Cont. Shelf Res., 26, 556– 560.

Puleo, J. A., and K. T. Holland (2001), Estimating swash zone friction coefficients on a sandy beach, Coastal Eng., 43, 25– 40.

Puleo, J. A., et al. (2000), Swash zone sediment suspension and transport and the importance of bore-generated turbulence, J. Geophys. Res., 105, 17,021–17,044.

Puleo, J. A., et al. (2002), Numerical modelling of swash zone hydrodynamics, paper presented at International Conference on Coastal Engineering, Am. Soc. of Civ. Eng., Cardiff, U. K.

Puleo, J. A., et al. (2003), Fluid acceleration effects on suspended sediment transport in the swash zone, J. Geophys. Res., 108(C11), 3350, doi:10.1029/2003JC001943.

Shen, M. C. and Meyer, R. E. Climb of a bore on a beach 3: Run-up. *J . Fluid Mech.* 16, 113- 125. 1963.

Shin, S, and D. Cox, Laboratory Observations of Inner Surf and Swash-zone Hydrodynamics on a Steep Slope, *Continental Shelf Research* Vol. 26, Issue 5 April 2006, 561-573.

Sleath, J. F. A. (1994), Sediment transport in oscillatory flow, in Sediment Transport Mechanisms in Coastal Environments and River, edited by M. Belorgey, R. D. Rajaona, and J. F. A. Sleath, World Sci., Hackensack, N. J.

Sleath, J. F. A. (1999), Conditions for plug formation in oscillatory flow, Cont. Shelf Res., 19, 1643–1664.

Suzuki, T. (2010), Spatiotemporal characteristics of Near-Bed Pressure Gradients on a Barred Beach, *Journal of Waterway, Port, Coastal, and Ocean Engineering*, Vol. 136, No. 6, November 1, 2010.

Svendsen, I. A. (2005), Introduction to Nearshore Hydrodynamics, Adv. Ser. on Ocean Eng., vol. 24, World Sci., Singapore.Thornton, E., Dalyrymple, T., Drake, T., Elgar, S., Gallagher, E., Guza, R., Hay, A., Holman, R., Kaihatu, J., Lippman, T., Ozkan Haller, T. 2000. *State of Nearshore Processes Research: II. Report Based on the Nearshore Research Workshop*, St. Petersburg, Florida. September 14-16, 1998. Technical report *NPS-OC-00-001*. Naval Postgraduate School, Monterey, California 93943

Turner, I.L., Masselink, G., 1998. Swash infiltration-exfiltration and sediment transport. J. Geophys. Res. 103, 30813-30824.

Appendix

COBRAS INPUT FILE

```
waveresuspension
 $numparam
   0.005,28.1,600.0,600.0<==delt,twfin,prtdt,pltdt
  0.3,1.0,3,1,1,2,1.0          <==alpha,beta,kl,kr,kt,kb,autot
   0,0.3,300.0                       <==npack,con,dmpdt
   0.01,0                    <==dtmax,idiv
   1.0d-3,0.39               <==erriccg,fcvlim
   1.0e-02,.false.           <==frctn,conserve
   3000,.true.,1             <==itmxiccg,sym
 $end
 $fldparam
   1.0e-06,0,-0.2867,-9.8058,0.0,0.0   <==xnu,icyl,gx,gy,ui,vi
   0.0d0, 1.0     <==psat,rhof
   0.,0.,0.,0.,0.,0.,0.,0.  <==uinf(1:4),vinf(1:4)
   0.0,0.0,0.0,0.0                   <==pbc(1:4)
 $end
 $mesh
   1.0,0.0,1<==make 1st and last 1 if use gui,else zero
   1,0.0,22,11,1100,1100
```

```
  0.01
  1,0.0,0.8,0.4,80,80
  0.005
 $end
 $obstcl
  0                    <==inputb
  1                    <==nobstype
  2                                        <==nporous(n-1)
  0.,0,-0.0292,-0.0833,0,0.,1,1        <==pa2,pa1,pb2,pb1
  0,0,0.2657,1.1862,1,1                          <==pc2,pc1,ipr
  0,0,0,0,0,0,0,0                <==pd2,pd1,pe2,pe1
  0,0,0,0,0,0,0,0              <==nxo,mxo,nyo,myo
 $end
 $freesurf
  0                              <==nfrsrf
  0., -0.0833   <==fa2(nfrsrf),fa1(nfrsrf)
0.,-1.   <==fb2(nfrsrf),fb1(nfrsrf)
  0.,1.6616,1.0<==fc2(nfrsrf),fc1(nfrsrf),ifh(nfrsrf)
  0.,0.                    <==fd2(nfrsrf),fd1(nfrsrf)
  0.,0.                    <==fe2(nfrsrf),fe1(nfrdrf)
  0,0                            <==nxf(nfrsrf),mxf(nfrsrf)
  0,0                            <==nyf(nfrsrf),myf(nfrsrf)
  0.42,.true.                  <==flht,upright
```

```
 $end
$wave parameter$
0.16,0.42,100<==aa,h0,ncenter
77,81,104,115,5,5.0
2.12
$output format$
0.0,0,1,1742,1,157,1,1,1,1,0        <==ts,tf,ib,ie,jb,je,ix,iy,lout,na,nm
17,10,18.55,26.55,26.60,26.65,26.70,26.75,26.80,26.85,27.00,27.5,28,28.5,29,29.5,30,
        30.5,0.0,50,0.0,0.1667<==nloc,xout(nloc),xxf,tend,prtdt_t
1.0,25,0.1667<==animationstart,animationend, framesps
$porous material information$
0                                <==npor
$turbulence model information$
4                                <==kemodel
0.05,1e-6,1
1                                            <==low turbulence level ends at this cell st
$boundary type$
0,1,0,1,1<==nweakref,nopen,islip,nrough,mirrort
0.00022,1
$sponge layer$
0
$free surface tracking method$
1                                <==nfree
$pollutant transport parameter$
```

```
2                                   <==npollutant
0.00022,1.34,1.0,1.0e-2,4.5,1.0e-6,3.6e-3
0.0,0.0,0.0,0.0,0.0,0.0
$restart controlling parameter$
0                                   <==nrs
$overtopping calculation$
0                                <==0:nocaluculaion
```